2014-11-01

Design and Analysis of Robotically-Controlled Minimally Invasive Surgical Instruments

Jordan D. Tanner
Brigham Young University

BYU ScholarsArchive Citation

Tanner, Jordan D., "Design and Analysis of Robotically-Controlled Minimally Invasive Surgical Instruments" (2014). *All Theses and Dissertations*. 6249.
https://scholarsarchive.byu.edu/etd/6249

Design and Analysis of Robotically-Controlled Minimally Invasive Surgical Instruments

Jordan D. Tanner

A thesis submitted to the faculty of
Brigham Young University
in partial fulfillment of the requirements for the degree of

Master of Science

Brian D. Jensen, Chair
Spencer P. Magleby
Larry L Howell

Department of Mechanical Engineering

Brigham Young University

November 2014

ABSTRACT

Design and Analysis of Robotically-Controlled Minimally Invasive Surgical Instruments

Jordan D. Tanner
Department of Mechanical Engineering, BYU
Master of Science

Robot-assisted minimally invasive surgery is used to perform intricate surgical tasks through small incisions using long, slender instruments. The miniaturization of these instruments is advantageous to both surgeon and patient because smaller instruments reduce trauma to surrounding tissue, decrease patient recovery times, and can be used in confined spaces otherwise inaccessible using larger instruments. However, miniaturization of existing designs is limited by friction between moving parts, the volume occupied by the end effector, and manufacturing and assembly constraints.

The objective of this work is to develop and analyze concepts that can be used in robot-assisted needlescopic surgery. The concepts are intended for instrument shafts no larger than 3 mm in diameter. An ideal concept is one with large ranges of wrist and gripping motion. Concepts should also minimize friction and swept volume while maintaining a focus on manufacturability and ease of assembly.

Multiple concepts were generated and evaluated using a tree classification scheme, proof-of-concept prototypes, and simplified mathematical models. Three unique concepts were further developed and tested—the Split CORE Grips, the Inverted Flexure Grips, and the Crossed Cylinders Wrist. The two grip concepts are instruments that incorporate one rotational degree of freedom and one gripping degree of freedom. The wrist concept incorporates two rotational degrees of freedom and could be coupled with a single DOF grip mechanism to form a functional instrument.

In addition to concept development, a variety of fabrication techniques were investigated to better understand the challenges that arise when designing and fabricating devices at the 3 mm scale. To augment existing techniques, a novel fabrication technique was developed which uses layers of lithographically patterned carbon nanotube (CNT) composite material to form a 3D part. This method was used to prototype some of the designs at a 1:1 size scale.

Keywords: minimally invasive surgical instrument, needlescopic surgery, robotics, carbon nanotube

ACKNOWLEDGMENTS

This work was made possible by a research grant from Intuitive Surgical, Inc. It has been a tremendous experience collaborating and establishing a partnership with experts in the field of robot-assisted surgery.

While I hope that my contributions to this work are of value to Intuitive Surgical, Inc. and to the scientific community, I suspect that my gains in terms of personal growth and professional development far surpass the value of any contributions I have been able to offer. This is largely because of the generous time, knowledge, and resources freely given by others assisting me with this work.

For this, I would like to specifically thank Dr. Brian Jensen for inviting me to work on this project and always being available to guide me in my growth and learning. From early in my undergraduate degree he has inspired me to accomplish things that I didn't otherwise consider myself capable of. Thanks also to Dr. Larry Howell and Dr. Spencer Magleby for taking time to hold weekly meetings to assess and guide this work, despite busy schedules and significant obligations in the college and department. Their examples of professionalism and excellence have shaped the way I view my own responsibilities as an engineer. A special thanks is also in order to Clayton Grames. His creativity, knowledge, and willingness to help wherever needed made him an invaluable resource on this project.

I wish to thank my mom and dad for their love and guidance, and for encouraging me to pursue my interest in engineering. Most importantly, I want to express appreciation to my beautiful wife, Krystle. She has given me her continued love and support despite my long hours at school. She has sacrificed so much of her own time and interests so that I could pursue this work. Finally, to my wonderful son, Nolan—thanks for helping me forget all the busyness of life and remember what's most important. You are the reason this is all worth it.

TABLE OF CONTENTS

LIST OF TABLES

LIST OF FIGURES

NOMENCLATURE

d_f	Cable offset distance on Split CORE mechanism
E	Modulus of elasticity
F_1, F_2	Input actuation forces on the Split CORE and Inverted Flexure mechanisms
F_{out}	Output force on Split CORE and Inverted Flexure mechanisms
F_p	Preload force applied to actuation forces
θ_j	Jaw angle of Split CORE mechanism
θ_r	Arc angle that defines the Split CORE base profile
L_j	Jaw length on the Split CORE and Inverted Flexure mechanisms
r_1	Radius of curvature of Split CORE base
σ'	Von Mises stress

CHAPTER 1. INTRODUCTION

1.1 Problem Statement

The intent of this project is to design a multiple-degree-of-freedom surgical instrument for use in needlescopic ($\leq$ 3 mm diameter) robot-assisted surgery. Current rigid body designs employ the use of pin joints, pulleys, and fasteners to achieve their intended motion. These designs are generally 5-12 mm in diameter. However, when scaling these designs to 3 mm, elements such as pulleys and pin joints become prohibitive due to challenges that arise at this size scale.

Manufacturing and assembly of these designs are perhaps the greatest challenges. Current designs rely on conventional machining methods (i.e. CNC milling) to produce each part. In a 3 mm design, this would require feature sizes as small as tens of micrometers. This is well beyond the capabilities of even the best CNC machines. An ideal design would minimize the number of parts in the assembly while maintaining a relatively simple geometry.

Friction is another challenge facing the design of smaller surgical tools. Friction is present in all rigid body mechanisms but is generally neglected in many macro-scale applications because it is small relative to other forces. However, when dealing with designs on the 3 mm scale, the magnitude of friction forces is comparable to the magnitude of forces used to actuate the mechanism. This becomes a serious problem when trying to precisely control or predict motion due to stick and slip behavior that occurs.

1.2 Background

Minimally invasive surgery (MIS) is used to perform a variety of complex medical procedures while reducing post-operative pain, scarring, recovery time, and the length of hospital stays. One particularly significant advance in the field of MIS is the use of robotics to more accurately and precisely control the instruments used in surgery. Intuitive Surgical Operations, Inc. has become a pioneer in this field by developing the *da Vinci* Surgical System. With nearly 2,800 *da Vinci* systems worldwide, surgeons were able to perform over 450,000 robotically-assisted procedures in 2012 [1]. Fig. 1.1 shows one of the current representative instrument designs.

The design is compact and efficient in providing high dexterity and a large range of motion. The Endowrist® is capable of producing pitch and yaw motions and the shaft to which it is attached is able to produce roll motions.

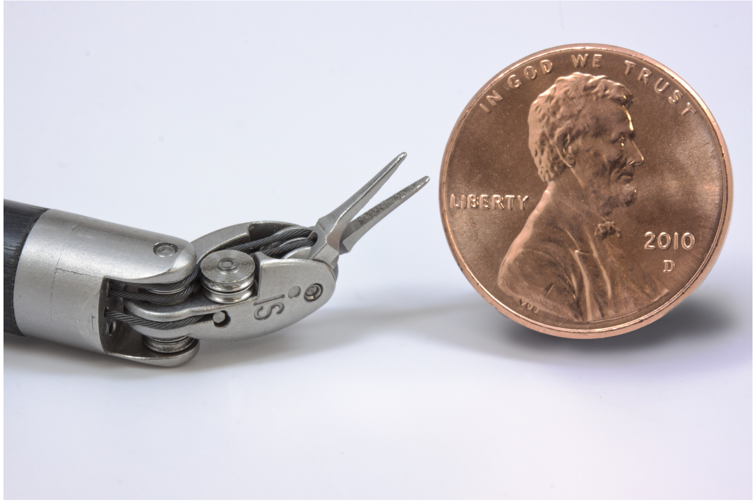

Figure 1.1: 8 mm Endowrist® design by Intuitive Surgical. Image courtesy of Intuitive Surgical, Inc.

In addition to rotational motion, the instrument can also be moved linearly by pivoting about the point of incision to produce two directions of lateral motion or by retracting/inserting the shaft farther to move laterally along the axis of the shaft.

One common type of MIS is laparoscopy, or procedures associated with organs and tissue located within the abdominal and pelvic regions. Laparoscopy had been used primarily for disease diagnosis in the early 20th century. However, it gained much wider support from the medical community in the late 1980's when German surgeon Erich Mühe successfully performed several laparoscopic cholecystectomies [2].

While laparoscopy is perhaps the ideal case for MIS because of the relatively large working space in the abdomen, there are a large number of medical procedures that must be performed in confined spaces. In many of these cases, MIS is not used because current instruments are too

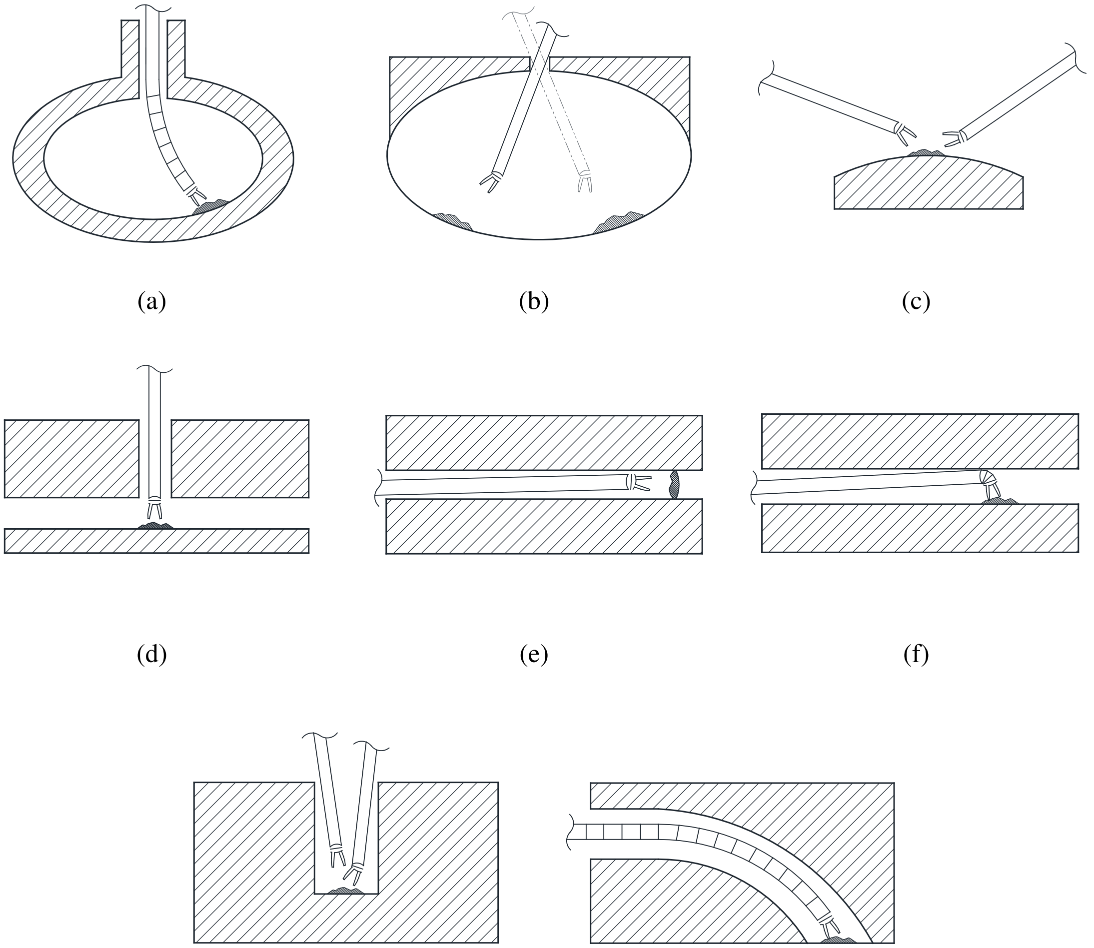

(a) (b) (c)

(d) (e) (f)

(g) (h)

Figure 1.2: Topologies that may be accessible through minimally invasive surgery.

large or simply pose too great a risk to patient safety. Small, robust instruments hold the potential to greatly increase the number of procedures that can be performed using MIS. Figure 1.2 shows simplified depictions of some working spaces that are currently encountered in MIS (a-c), and other spaces where MIS could be used given the appropriately sized instruments (d-h). For example, arthroscopy, or MIS joint repair, is performed in small working spaces with restricted motion of the end effector. Other procedure sites, such as those performed at the base of the brain, have small access points in the nose or mouth and therefore require instruments with small cross sections.

1.3 Thesis Objectives

A variety of minimally invasive surgical instruments have been created to grasp tissue, excise tumors and cysts, suture openings, lift organs, perform cautery, etc. This research will focus specifically on an instrument capable of gripping a needle for suturing. However, the resulting designs will likely be suitable for other functions by making small modifications to the underlying elements that give the mechanism its function.

The majority of instruments currently available rely on rigid-body construction. Elements such as pin joints and pulleys offer very predictable motion that is relatively easy to analyze. Unfortunately, the scalability of such mechanisms is limited by several factors, particularly when moving from the current 5 and 8 mm designs to a 3 mm design. Friction between moving components in the instrument is among the primary challenges associated with smaller designs. Another is manufacturing and fabrication feasibility.

Two techniques have been used to address these challenges. One technique is to use compliant mechanism design rather than rigid-body design. Compliant mechanisms provide a way to mitigate friction and wear by reducing or eliminating parts that move relative to one another. Additionally, compliant mechanisms generally involve fewer parts than rigid body mechanisms. By reducing the part count of a particular design, the fabrication time and difficulty will also be reduced.

The second method involves designs that rely on rolling motion in order to eliminate nearly all sliding friction. The Compliant Rolling-Contact Element (CORE) is the basis of these designs [3]. The proposed work accomplishes the following objectives:

1. A survey of prior art regarding wrist and gripper mechanisms.
2. Investigation of suitable materials and fabrication techniques.
3. Development of analytical models for a variety of designs of wrists and grippers. This allows comparison between the designs for the following attributes:
    - Range of motion
    - Stiffness and load capacity
    - Scalability

    - Ease of fabrication

4. Prototyping and testing of top performing designs and comparison to the analytical models.

1.4 Thesis Accomplishments

1.4.1 Prior Art Survey

An extensive survey of prior art relating to this project has been performed. The majority of work published regarding minimally invasive surgical instruments refers to rigid body mechanism designs. Within the 5-12 mm range are instruments with end effectors that can pivot about two axes and produce gripping motion. Examples include the Easy Grasp by Wang et al. [4], the surgical device by Whitman [5], the DragonFlex instrument by Jelinek [6], and the Endowrist® by Intuitive Surgical, mentioned previously.

There has also been significant work done on wrist and gripper designs for other industries and applications, but on different size scales. This work has provided a starting point from which to generate new ideas. For example, the microfabrication industry requires manipulation of extremely small, sensitive parts. A variety of micro grippers have been developed for this purpose and rely on compliant motion [7, 8]. Automated automobile manufacturing is another field where part manipulation is used. This is achieved using robotic wrists with two or more degrees of freedom to move and assemble parts. Both of these examples are outside of the size range of this project, but both contain product concepts that have been used to generate new ideas that satisfy the design constraints of this project.

1.4.2 Materials and Fabrication Techniques

In selecting a good design, part of the product development process involves selecting suitable materials for the design and also feasible machining and fabrication techniques. Current designs are produced using a combination of conventional machining (i.e. CNC milling) for some parts and metal injection molding for others. At the desired size scale, conventional machining begins to reach its limits in terms of precision and tolerances. This is also true of metal injection molding because the molds are typically made using conventional machining techniques.

For this reason, other fabrication techniques have been explored. One such process that has been demonstrated is the use of photolithography to create thin planar structures that can be stacked together in such a way that they form a 3D structure. The use of photolithography allows for extremely high precision and can be used in batch fabrication. Fig. 1.3 shows the Crossed Cylinders wrist mechanism fabricated from carbon nanotubes using the process described.

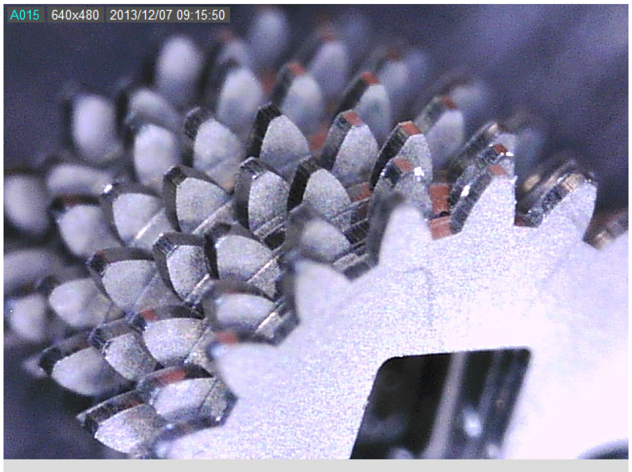

Figure 1.3: A mechanism fabricated from carbon nanotubes using a multilayer process to produce a 3D shape.

1.4.3 Analytical Models

To produce accurate, precise motion using robotic controls, it is necessary to understand the kinematic behavior of the mechanism. Any coupling that may occur between degrees of freedom must be understood so that it can be accounted for in the driver controls. Analytical kinematic models have been created for each of the selected concepts. These models were used in conjunction with finite element analysis to assess the stress response for the desired motion.

1.4.4 Prototyping and Design Validation

Proof-of-concept prototypes were created for most of the concepts generated in the initial development stages to demonstrate the functionality of a design and to determine weaknesses that exist. The designs were screened and compared against the desired functional specifications so

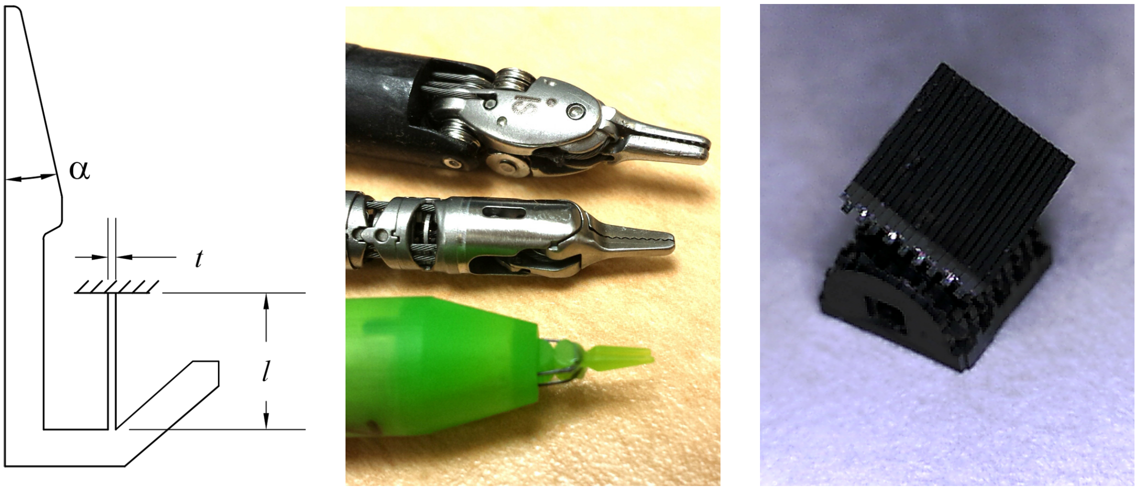

(a) (b) (c)

Figure 1.4: Depiction of the Inverted Flexure Grips concept (a) and prototypes of the Split CORE Grips (b), and the Crossed Cylinders Wrist (c) developed for a 3-mm minimally invasive surgical instrument.

that the best designs could be recognized. At this point, higher fidelity models and prototypes were created for testing and comparison. The majority of the prototypes were built at a 10:1 scale of the intended mechanism. Later, 1:1 scale prototypes were built, assembled and tested on actual robotic instrument shafts.

1.5 Thesis Contributions

The objective of this project was to develop concepts that meet the desired functional requirements of a minimally invasive surgical instrument. Three concepts were ultimately selected as candidate solutions, the Inverted Flexure Grips, the Split CORE Grips, and the Crossed Cylinders Wrist. Models of these concepts are shown in Fig. 1.4. A novel fabrication technique has also been developed as a possible method for building these concepts. The outcomes of the work have been compiled and delivered to Intuitive Surgical, Inc. in a mid-contract and end-of-contract report, along with a number of intermediate reports.

In addition to fulfillment of the research contract with Intuitive Surgical, Inc. another objective of this work was to contribute findings and developments to the scientific community through publications and patent applications. Chapter 5 was accepted and presented at the 3rd Conference on Microactuators and Micromechanisms in Timisoara, Romania, 2-4 October, 2014. Chapter 6 has been submitted and is currently under review for the ASME Journal of Mechanisms and Robotics. Provisional patent applications have also been submitted for both the Split CORE Grips and the Crossed Cylinder Wrist concepts.

CHAPTER 2. PRIOR ART

2.1 Introduction

A variety of mechanisms exist that produce grasping and/or wrist motion. The intent of this chapter is to provide an overview of the literature and prior art available which describes these mechanisms. The chapter provides ideas that were used to facilitate design activities. Although the chapter will focus on mechanisms used in laparoscopic surgery, not all the findings reported here are exclusive to laparoscopy, and some are not used in the medical industry at all.

Following a description of the existing technology, an overview of the concept generation process is given. This process resulted in a pool of candidate solutions that were classified and filtered based on their performance characteristics. From this classification and filtering process we selected three unique designs for further development and analysis.

In an effort to organize the wide array of mechanisms, they are categorized by size and degrees of freedom of the end effector. Figure 2.1 shows a X-Y coordinate plane subdivided into four quadrants, used to illustrate this simple classification scheme. Approximate sizes and degrees of freedom for each quadrant are also shown. The divisions between quadrants are somewhat arbitrary and, obviously, not to scale; but, these divisions provide a good representation of work that has been done in the past, where this project fits in relation to other works, and areas of opportunity that have yet to be explored.

2.2 Prior Art and Literature

2.2.1 Quadrant I

Quadrant I, shown in Figure 2.1, contains designs which are limited in mobility and are large relative to designs found in the lower quadrants. These designs are simple and generally quite robust. The majority of these mechanisms are strictly limited to grasping and do not involve any

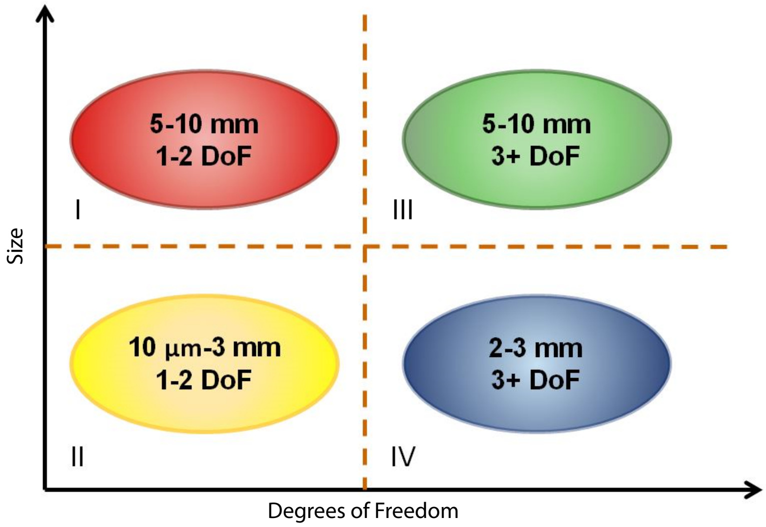

Figure 2.1: Quadrants I-IV used to classify and describe grasping and wrist mechanisms based on size and degrees of freedom.

wrist motion. Because size is not a major design constraint we see a variety of mechanism types that fit within three subclass—rigid body, partially compliant, and fully compliant mechanisms. Rigid body mechanisms are those that incorporate rigid (or assumed to be rigid) elements such as links, pins, pulleys, etc. to achieve motion. In compliant mechanisms, all motion is produced by the deflection of flexible elements. Lastly, partially compliant mechanisms are simply a combination of rigid and compliant elements.

Representative examples of rigid body mechanisms are shown in Figure 2.2. Figure 2.2(a) illustrates a mechanism known as the Laparoscopic Dual Grasper which is actuated by a rod running along the shaft. The rod opens or closes a pair of jaws which pivot about a common axis and whose motion is coupled. The next example, Figure 2.2(b), is an electrosurgical instrument used to seal tissue. It also uses a push/pull rod to actuate the opening and closing of the jaws.

Figure 2.3 illustrates two mechanisms that are partially compliant. The first, Figure 2.3(a), is a pair of jaws that pivot about a pin joint while the forces required for actuation are transmitted through flexible members. The intent of this type of design is to mitigate the backlash and the friction losses associated with transmitting force through a rigid body mechanism [11]. A similar design described in [12] also applies an actuation force at the outer surface of the jaws, but the jaws pivot about a living hinge rather than a rigid hinge. The second mechanism, shown in Figure 2.3(b),

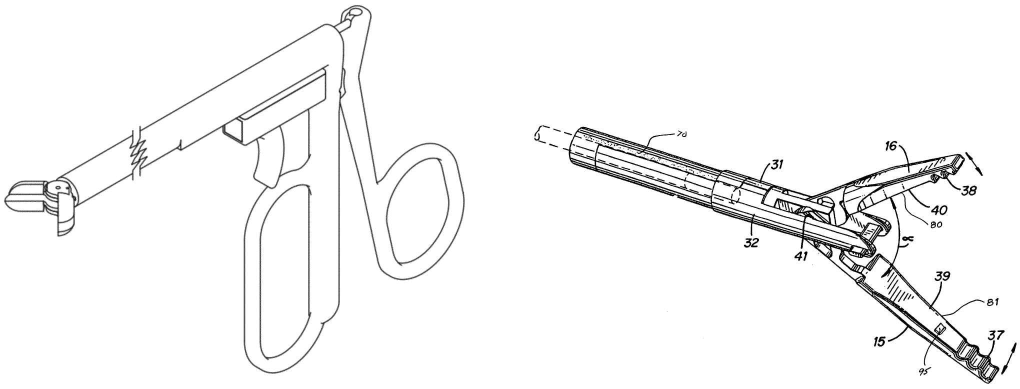

(a) (b)

Figure 2.2: Rigid body grasping mechanisms: (a) The Laparoscopic Dual Grasper [9], (b) An electrosurgical tissue sealing mechanism [10].

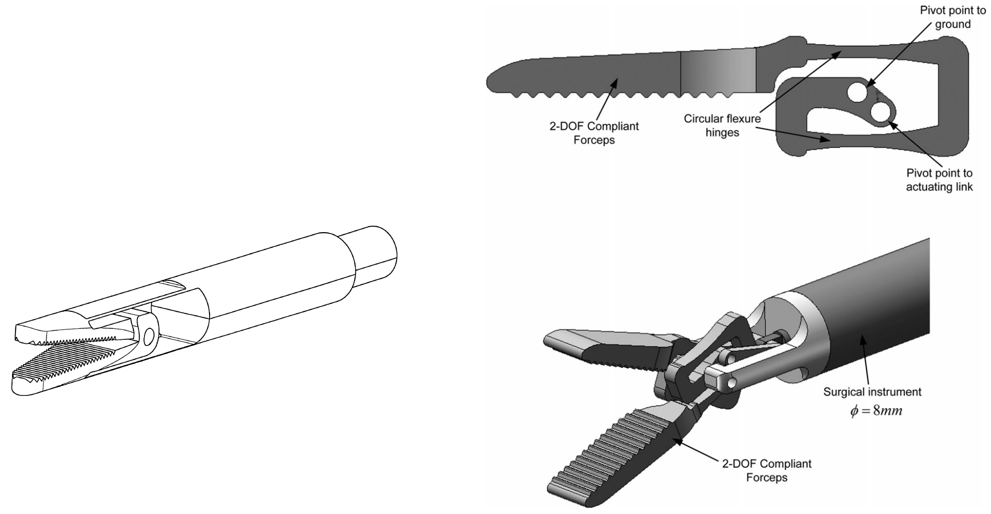

(a) (b)

Figure 2.3: Partially compliant grasper mechanisms: (a) A grasper composed of pivoting jaws actuated by flexible members [13], (b) Jaws with a common pivot but independent motion caused by two compliant members joined in series [14].

consists of two jaws that pivot about a pin joint. Two flexure hinges are integrated into the design of each jaw for the purpose of measuring grasping forces by using the compliance characteristics of the jaws.

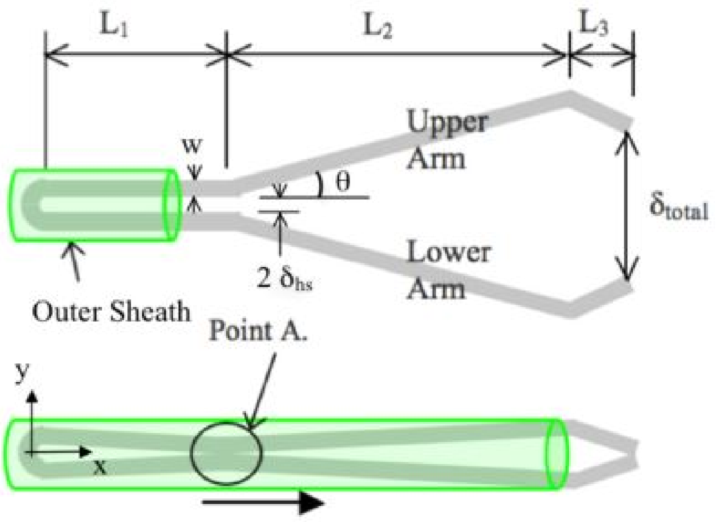

Figure 2.4: Fully compliant graspers [16, 17].

The final subclass within this category consists of fully compliant mechanisms and can be represented by the design in Figure 2.4, which consists of a simple set of jaws with a sheath surrounding them. As the jaws move into or away from the sheath they are forced closed or able to spring open, respectively. Because of the simplicity of this design, it can be scaled down to small sizes. The MiniLap instruments by Stryker® (San Jose, CA) rely on a similar design and are approximately 2.4 mm in diameter [15]. However, as in the previous designs, the MiniLap instruments only provide grasping motion.

Oftentimes, compliant designs can be inspired by mechanisms found in nature. This concept is used in the designs described in [18–20] which are able to grasp and manipulate small objects or surfaces. Also, while each of the examples illustrated in the figures thus far are actuated by rods or cables of some form, there are designs that rely on other forms of actuation. Shape memory alloys are used to produce motion in some designs, [21–25], and piezoelectric elements are used in yet other designs [18, 26–29].

2.2.2 Quadrant II

Categorized in quadrant II are designs that are significantly smaller than those in the first quadrant but whose mobility is still limited to one or two degrees of freedom. Many, but not all, designs found in this category must be produced using techniques other than conventional machining. Some of these designs rely on lithographic patterning, [30–33], and chemical etching or deep reactive ion etching (DRIE), [34, 35], to achieve micron and sub-micron resolution. Others are fabricated using laser machining or micro-EDM [36].In general, these types of mechanisms have high accuracy and resolution but produce rather small forces at the grasping tips [37–39].

Two representative examples are those shown in Figure 2.5. The first example, Figure 2.5(a), is a silicon micro-gripper that is electrothermally actuated to provide the desired motion. It is approximately 3 mm wide and is capable of grasping objects on the order of 25 μm. The second example, shown in Figure 2.5(b), is piezoelectrically actuated and has a grasping range of up to 800 μm. It was designed with the intent of grasping and manipulating fibers in the fiber optics industry. Both designs rely on thin compliant flexures to achieve the desired grasping and releasing motion.

Another mechanism defined within this category is the Microrobotic Wrist. This design is manufactured using deep reactive ion etching (DRIE) and lithography electroplating molding (LIGA). It provides two degrees of wrist motion, rather than a grasping motion. Figure 2.6 shows an assembled view of the wrist mechanism. It consists of three compliant legs attached to an end effector base. Forces are applied independently to the three legs using long, thin push rods and pulling wires causing the rotation of the end effector base.

2.2.3 Quadrant III

Transitioning from Quadrant II to III involves an increase in degrees of freedom. With more degrees of freedom, designs begin to combine grasping and wrist motion and, consequently, become more complex. There already exist several highly dexterous robotic hands that involve wrist and finger motion such as those described in [41]. However, these are on the scale of a human hand. As these mechanisms scale to smaller sizes (5-10 mm), many design constraints

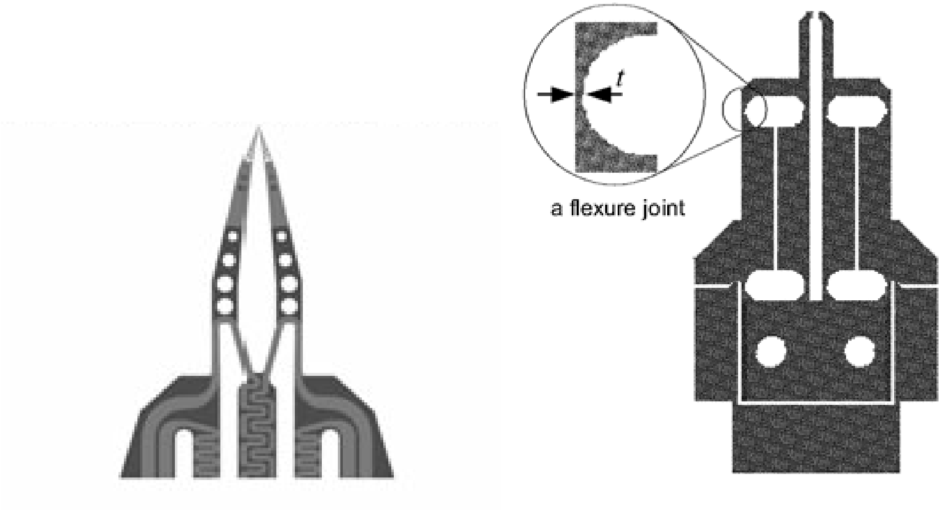

(a) (b)

Figure 2.5: Miniature compliant grasper mechanisms: (a) Silicon micro-gripper controlled by electrothermal actuation [7], (b) Miniature gripper system with piezoelectric actuation for fiber optic handling [8].

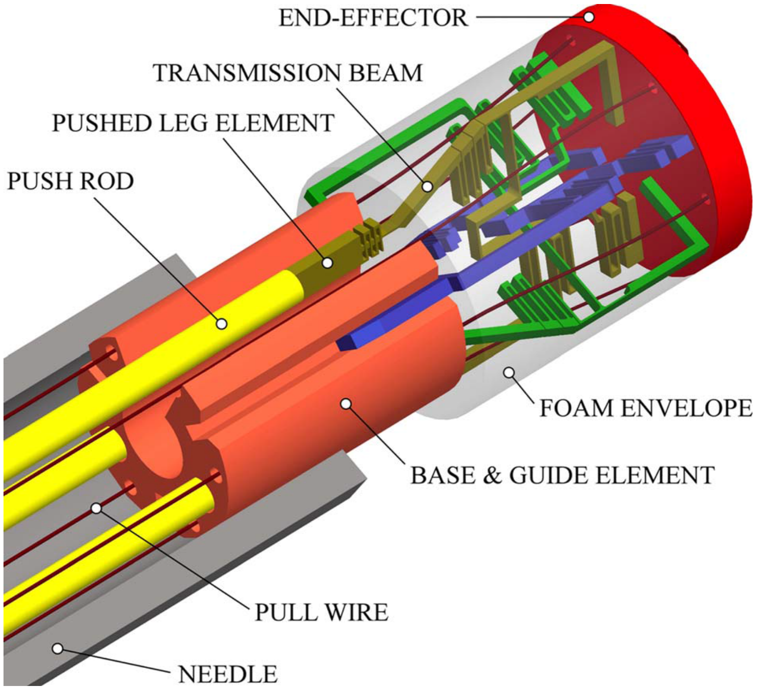

Figure 2.6: A 2-DoF microwrist employing three compliant legs assembled together [40].

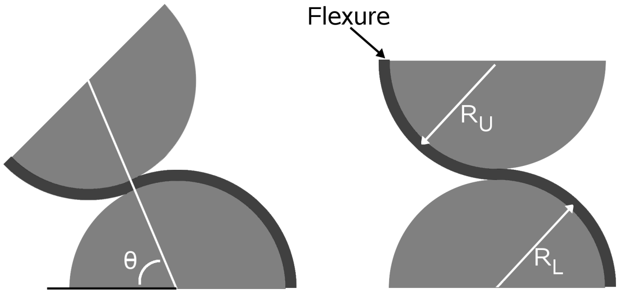

Figure 2.7: A compliant rolling-contact element (CORE), [3].

arise, the most obvious being simply fitting all the components into a more compact space. The grasper function and the wrist function must be capable of acting simultaneously without impeding the motion of the other. In some cases an effort is made to decouple the two functions such as in [42] and [43]; however, in many designs there is a certain level of coupling, in which case the kinematics must be understood to accurately produce desired motions.

In general, the mechanisms in this category provide high dexterity within a relatively compact space [44,45]. However, another challenge that is presented when combining multiple degrees of freedom relates to the working volume of the mechanism. As the wrist rotates from one extreme position to another, it sweeps the grasping jaws through a volume of space defined by the distance of the jaws from the center of rotation of the wrist. Ideally, this working volume will be minimized to provide a surgical instrument that is not only highly dexterous but also capable of operating in small spaces. One method described in [46] utilizes a compact joint called a compliant rolling-contact element (CORE) to produce a wrist that occupies little working volume [47]. An image of the CORE element is shown in Figure 2.7. Another method is to use a ball and socket joint [48].

Representative examples that fit this category are shown in Figures 2.8 and 2.9. The DragonFlex, shown in Figure 2.8, is a mechanism with a series of joints that are held together by cables. Each joint is associated with one degree of freedom at the end effector. There is an equal number of joints at the operator end such that for a given movement caused by the operator, the same

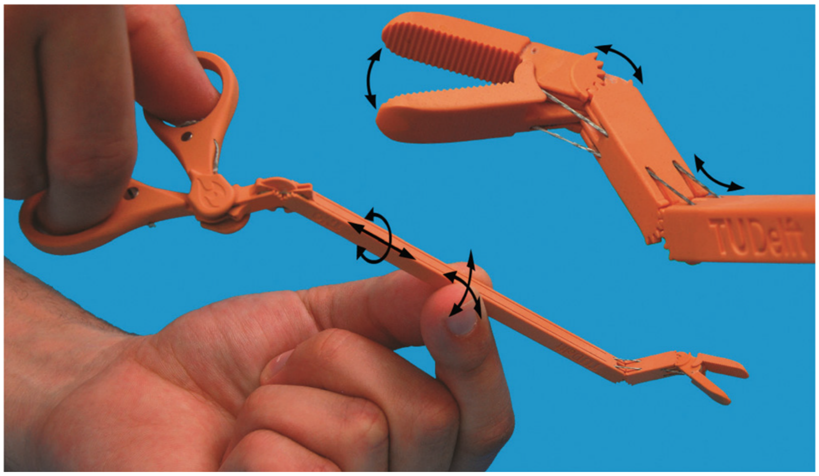

Figure 2.8: The DragonFlex laparoscopic instrument [6].

movement is produced at the corresponding joint at the end effector. Thus, by using cables, pin joints, and gear teeth at the joints, this fully rigid-body mechanism is able to produce three degrees of freedom at the end effector [6].

Two mechanisms that are quite similar in function but different in design are the EndoWrist by Intuitive Surgical® (Sunnyvale, CA) and the grasper based on planetary gear theory described in [42]. These two designs are shown in Figure 2.9(a) and Figure 2.9(b), respectively. Both designs are actuated by a number of cables. However, the EndoWrist uses pulleys for wrist and grasper articulation while the other design uses a set of planetary gears to fully decouple the motion of the wrist and grasper. Both designs maintain the grasper relatively close to the center of rotation of the wrist, thus providing a fairly small working volume. In contrast, the DragonFlex jaws, as well as the mechanism jaws described in [4,5,49–51], are somewhat farther from the rotation of the wrist, causing them to occupy a larger amount of space for movement.

We see in these examples that the mechanisms all consist of rigid body links and joints. This is likely because size is not yet so small as to prevent reasonable assembly of the individual components.

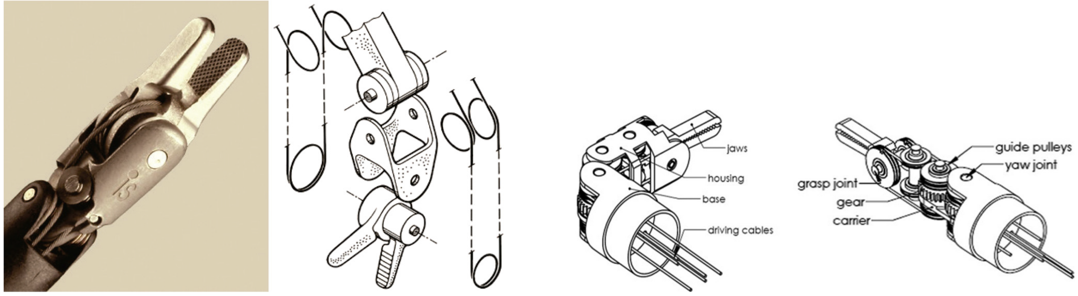

(a) (b)

Figure 2.9: Wrist and grasper designs with 3+ degrees of freedom: (a) The EndoWrist by Intuitive Surgical (image courtesy of Intuitive Surgical, Inc.), (b) Grasper and wrist with decoupled motion [42].

2.2.4 Quadrant IV

Finally, in the last quadrant we define designs which are less than 3 mm in diameter and have three or more degrees of freedom at the end effector. Ultimately, this is also where solutions for this project will be categorized. Throughout the literature review, there were no works that could appropriately be placed within this category. Many new challenges are present in this area that are not as pertinent in quadrants I and III. For example, manufacturing techniques used in the 5-10 mm range are less reliable when dealing with parts smaller than 3 mm. The differences in manufacturing techniques between quadrants I and II are evidence of this. In addition to manufacturing, assembly of individual parts must be considered.

Another challenge that must be addressed relates to the effects of scaling, particularly friction and mechanism stiffness. This is one possible reason that a shift from rigid body to compliant mechanisms can be seen in the other three areas as designs become smaller.

2.3 Concept Generation

An understanding of existing technologies provided a base of knowledge from which to develop concepts for a 3 mm instrument. The objective of the concept generation process was to create an assortment of ideas with sufficient depth and breadth to fill the design space. This resulted in many unique concepts, each tailored to address the challenges of miniaturization described in Chapter 1.

A tree classification scheme was used to sort each of the ideas into groups and subgroups based on common characteristics. This made it simple to see areas where there was an abundance of ideas, and other areas where new concepts were lacking. It also led to additional concepts that consisted of combinations of earlier ideas. The following performance metrics were used to evaluate each concept and help identify those with the greatest strength and potential:

- Manufacturability
- Minimizing swept volume
- Range of motion (target range of ±90°)
- Ease of integration into the existing robotic interface

From this process a number of proof-of-concept prototypes were made to further evaluate the potential candidate solutions using the same metrics mentioned previously. Ultimately, three concepts were selected for further analysis and testing. These are described in subsequent chapters.

2.4 Conclusion

In summary, there is a wide variety of mechanisms that are capable of producing either grasping motion or wrist motion, or both. The methods for actuation also vary considerably; although, because many of them are intended as laparoscopic instruments, they are most commonly actuated using long thin rods or cables running inside of the instrument shaft.

One trend that can be observed in this report is that as the instruments become smaller, the designs begin to shift from rigid body mechanisms to compliant mechanisms. This transition may be attributed to a number of factors that must be addressed. As mentioned previously, in smaller designs assembly becomes more difficult if there are many parts involved. Compliant mechanisms typically have significantly fewer parts to assemble. Also, the scaling effects that emerge when reducing the size of a mechanism increase the relative size of friction, which impedes the motion of the wrist and grasper. Compliant mechanisms experience less friction than rigid body designs and therefore have less resistance to motion.

A shift is also observed in the manufacturing and fabrication methods when decreasing the size of instruments. Lithographic patterning and etching proves to be a popular technique, likely because it provides high resolution and can be used with a variety of materials.

Referring to the graph in Figure 2.1 used to classify the literature and prior art, we see that there is little work done in the area of small, highly dexterous mechanisms (Quadrant IV). With such an open design space in which to work, there are many challenges that need to be addressed. Along with those challenges, there are also many opportunities to explore and pursue a variety of possible solutions. This was demonstrated in the concept generation and evaluation process as three designs were selected as those considered to offer the greatest potential moving forward.

CHAPTER 3. DESIGN ANALYSIS OF A SPLIT CORE GRIP MECHANISM

3.1 Introduction

The Split CORE is a derivation of the traditional CORE (Compliant Rolling-Element) Joint that involves joining two half cylinders with flexures [3]. The Split CORE replaces the half cylinders with truncated joints to reduce the size of the joint. Consequently, this also limits the range of motion to ±90 degrees which is considered acceptable for many applications. In place of flexures the Split CORE uses the input actuation force to maintain compressive contact between the different elements. Additionally, the top half of the joint is split in two to create two distinctly controllable surfaces where individual jaws are mounted. This creates a two-degree-of-freedom gripping mechanism—one rotational degree of freedom, and another degree of freedom associated with the opening and closing of the jaws.

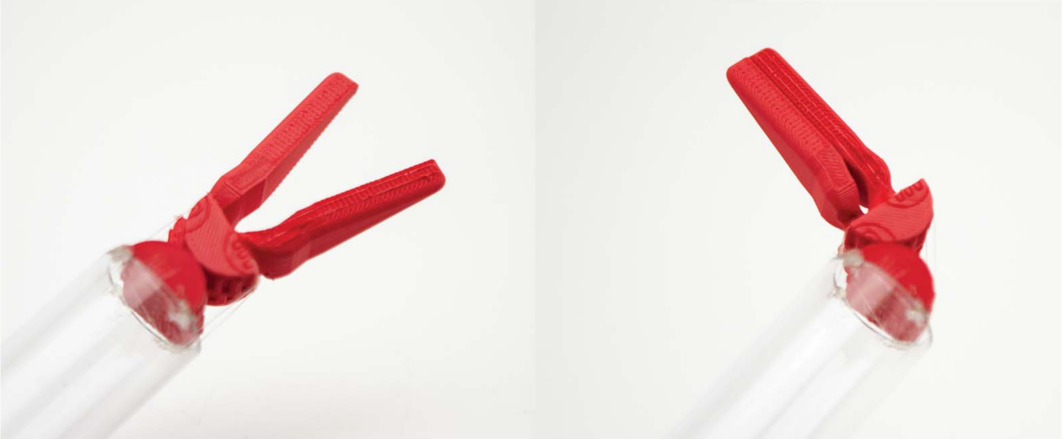

Figure 3.1: A 10:1 scaled prototype demonstrating two degrees of freedom.

The curved surfaces of the upper and lower rolling segments consist of two rows of gear profiles which prevent slip between the two segments and allow precise control of the gripper locations. The curved surfaces also include non-geared areas which support the compressive loads

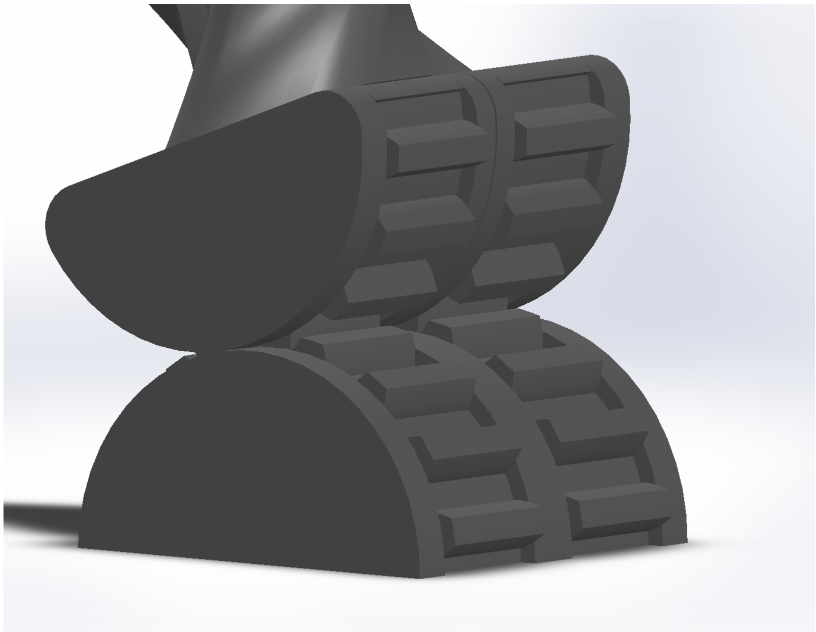

Figure 3.2: CAD model of the Split CORE mechanism showing the gear profiles and flat regions of the rolling surfaces.

associated with gripper motion and holding the assembly together. There are three distinct non-geared regions as shown in Fig. 3.2. These regions are included in the design so that all compressive loads are transferred away from the gear profiles which would otherwise experience higher stresses because of smaller cross-sections and stress concentrations.

3.2 Design Analysis

This analysis defines both the position of the jaws and the relationship between the input and output forces of the Split CORE mechanism. The output force is defined as the force acting orthogonal to the tip of the jaw while the input force is defined as a force at the edge of the top half of the joint and acts toward the edge of the lower segment. The output force models the reaction force applied by whatever the mechanism is gripping. The input force is provided by cabling routed from the mechanism through the tool shaft and to the base housing where the input torque is provided.

3.2.1 Model Geometry

The motion of the Split CORE is most easily modeled when compared to the motion of the traditional CORE joint. The traditional CORE joint is modeled as two half cylinders—a fixed lower segment and a free upper segment which rolls along the curved surface of the lower segment. This is shown in Fig. 3.3 by the dashed lines. The proposed design (Split CORE model) is based on the same principle but uses a smaller portion of the circular arc to reduce the size of the joint, is shown in Fig. 3.3 by the solid lines. The arcs of both the traditional CORE model and the Split CORE model have the same radius of curvature, r_1, and are concentric. The centers of the lower and upper segments are labeled as O and A, respectively. Although neither of the centers physically exist on the Split CORE model they are used as reference points because they simplify the derivations of equations of motion and force output.

The angle θ_r is used to describe the size of the arc used in the design. For example, if θ_r is equal to 90° the result would be equivalent to the traditional CORE joint. If θ_r is equal to 45° the resulting mechanism would look similar to the one shown by solid lines in Fig. 3.3.

The parameters of interest in this design are the output force at the jaws, F_{out}, the angle of the jaws, θ_j, and the required input forces, F_1 and F_2. The principle of virtual work is used to determine these input forces for any given values of F_{out} and θ_j. The angle used to describe the point of contact between the upper and lower segments (θ_c) is also used but can be described as a function of the jaw angle by the following relation:

$$\theta_c = \frac{\theta_j}{2} \tag{3.1}$$

All angles shown in Fig. 3.3 are defined as positive counter-clockwise from the y-axis, and the origin of the coordinate system is at point O as shown. Another coordinate system, x'-y', is also shown. This system will be used along with a rotation matrix to define the location and direction of the input forces in terms of the x-y coordinate system. The origin of the x'-y' coordinate system is point A.

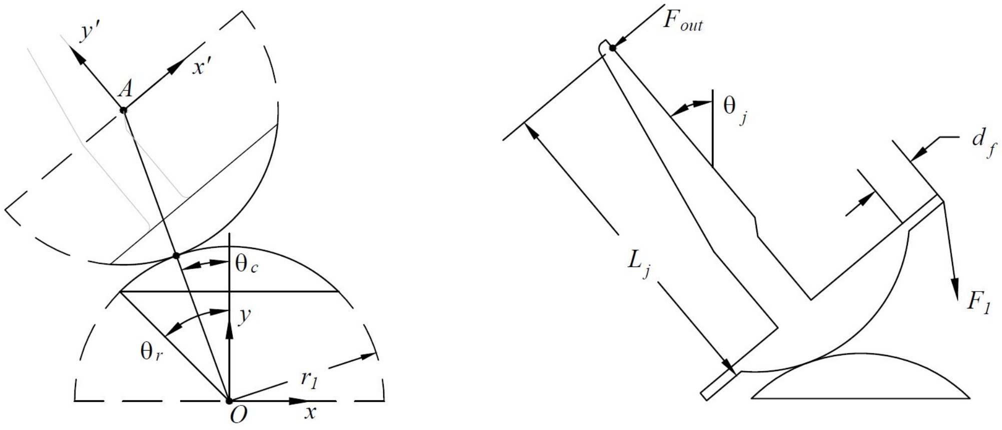

Figure 3.3: The geometry and parameters used in deriving the equations of motion and force output for the Split CORE mechanism.

3.2.2 Input Force and Mechanical Advantage

Two input forces exist in this design, F_1 and F_2. An assumption can be made regarding the relationship between these two forces. If the actuating cables attached at the points of F_1 and F_2 are connected to a common spool then as a force is applied to one cable the force in the opposite cable goes to zero. For example, under this assumption, if F_1 equals 2 N then F_2 is zero. In addition to this assumption Fig. 3.3 shows that for any nonzero value of F_{out}, F_1 will also be nonzero, and consequently F_2 will be zero. This is because F_1 is the only force that can balance the system. If considering the other jaw in the assembly (not shown in Fig. 3.3), for any nonzero value of F_{out}, F_2 would be nonzero and F_1 would be zero. The derivations that follow apply to the case shown in Fig. 3.3 where F_2 is zero. However, the same approach can be used to consider the case for the opposite jaw.

The method of virtual work can be used to determine the magnitude of F_1 for given values of F_{out} and θ_j. The first step in calculating the virtual work in the system is choosing a generalized coordinate. The jaw angle, θ_j, is a convenient parameter because it is used to describe the position of the jaw, and because the expression for F_1 will be derived as a function of θ_j. Therefore, θ_j will be used as the generalized coordinate. Next, each of the applied forces are written in vector form in terms of the generalized coordinate. The input force in this model is placed at a distance d_f from the corner of the upper segment and points toward a point a distance d_f from the corresponding corner of the lower segment. This assumption is based on the idea that cables provide the input forces and route around the lower geometry before entering the shaft and connecting to the control interface at the opposite end of the instrument. The reason for placing the input force a distance from the corner is to increase the moment arm, and consequently the mechanical advantage. This is particularly important when the point of rolling contact is near corners of the segments (i.e. as θ_c approaches θ_r). However, in this configuration it is also important to address any interference that may result from placing the forces and cables at these locations. Using this assumption the directions of the forces are shown in Eqs. 3.2 and 3.3 for F_{out} and F_1, respectively.

$$\mathbf{F_{out}} = F_{out}\left(-\cos\theta_j\hat{\mathbf{i}} - \sin\theta_j\hat{\mathbf{j}}\right) \tag{3.2}$$

$$\mathbf{F_1} = F_1\left(\sin\frac{\theta_j}{2}\hat{\mathbf{i}} - \cos\frac{\theta_j}{2}\hat{\mathbf{j}}\right) \tag{3.3}$$

Next, position vectors are written from the origin, O, to each of the applied forces. The vector describing F_{out} is fairly simple to describe in terms of θ_j and is given by Eq. 3.4. The other vector is more complicated because it lies at some point on the arc determined by θ_r and that point sits somewhere in space determined by θ_j. To simplify the derivation of the position vector $\mathbf{F_1}$, two vectors can be summed together—one from point O to point A, and the second from point A to the location of force application. This second vector can be described in the x-y coordinate system using a rotation matrix. This results in the following equation for the position of F_1.

$$\mathbf{Z_{out}} = \left[-2r_1\sin\frac{\theta_j}{2} - \left(L_j - r_1\cos\theta_r\right)\sin\theta_j\right]\hat{\mathbf{i}} + \left[2r_1\cos\frac{\theta_j}{2} + \left(L_j - r_1\cos\theta_r\right)\cos\theta_j\right]\hat{\mathbf{j}} \tag{3.4}$$

$$\mathbf{Z_1} = -2r_1\sin\frac{\theta_j}{2}\hat{\mathbf{i}} + 2r_1\cos\frac{\theta_j}{2}\hat{\mathbf{j}} + \begin{bmatrix}\cos\theta_j & -\sin\theta_j \\ \sin\theta_j & \cos\theta_j\end{bmatrix}\begin{bmatrix} r_1\sin\theta_r\hat{\mathbf{i}} \\ -r_1\cos\theta_r\hat{\mathbf{j}}\end{bmatrix} \tag{3.5}$$

Equation 3.5 can be expanded to its $\hat{\mathbf{i}}$ and $\hat{\mathbf{j}}$ components and then simplified. Doing this results in Eq. 3.6.

$$\mathbf{Z_1} = \left[-2r_1\sin\frac{\theta_j}{2} + r_1\sin\left(\theta_j + \theta_r\right)\right]\hat{\mathbf{i}} + \left[2r_1\cos\frac{\theta_j}{2} - r_1\cos\left(\theta_j + \theta_r\right)\right]\hat{\mathbf{j}} \tag{3.6}$$

The next step is to determine the virtual displacement of each point of force application by calculating the partial derivatives of Eqs. 3.4 and 3.6 with respect to the generalized coordinate.

$$\delta \mathbf{Z_{out}} = \left\{ \left[-r_1 \cos\frac{\theta_j}{2} - \left(L_j - r_1 \cos\theta_r\right)\cos\theta_j \right] \hat{\mathbf{i}} + \left[-r_1 \sin\frac{\theta_j}{2} - \left(L_j - r_1\cos\theta_r\right)\sin\theta_j\right] \hat{\mathbf{j}} \right\} \delta\theta_j \tag{3.7}$$

$$\delta \mathbf{Z_1} = \left\{ \left[-r_1 \cos\frac{\theta_j}{2} + r_1 \cos\left(\theta_j + \theta_r\right) \right] \hat{\mathbf{i}} + \left[-r_1 \sin\frac{\theta_j}{2} + r_1 \sin\left(\theta_j + \theta_r\right) \right] \hat{\mathbf{j}} \right\} \delta\theta_j \tag{3.8}$$

The virtual work associated with each force is determined by calculating the dot product of each force vector (Eqs. 3.2 and 3.3) and its respective virtual displacement vector (Eqs. 3.7 and 3.8).

$$\delta W_{out} = F_{out}\left(r_1 \cos\frac{\theta_j}{2} - r_1\cos\theta_r + L_j \right)\delta\theta_j \tag{3.9}$$

$$\delta W_1 = -F_1 r_1 \sin\left(\theta_r + \frac{\theta_j}{2}\right)\delta\theta_j \tag{3.10}$$

The total virtual work in the system is calculated by summing each component of virtual work from Eqs. 3.9 and 3.10. For a system in equilibrium, the principle of virtual work states that the total virtual work is equal to zero. This makes it possible to rearrange the equation to determine F_1 for various values of F_{out} and θ_j.

$$0 = \left[F_{out}\left(r_1\cos\frac{\theta_j}{2} - r_1\cos\theta_r + L_j\right) - F_1 r_1 \sin\left(\theta_r + \frac{\theta_j}{2}\right)\right] \tag{3.11}$$

$$F_1 = \frac{F_{out}\left(\cos\frac{\theta_j}{2} - \cos\theta_r + \frac{L_j}{r_1}\right)}{\sin\left(\theta_r + \frac{\theta_j}{2}\right)} \tag{3.12}$$

3.2.3 Including a Preload Force

It may be desirable in some cases to apply a certain amount of preload force to the points of force application (Fig. 3.3). This would reduce any effects of backlash that may occur and would ensure higher levels of control over the motion of the mechanism. If an equal preload force is applied to both sides of the mechanism (i.e. equal preload in both actuation cables) then the changes to the previous derivations are relatively simple. The input force term, F_1, in Eq. 3.11 is replaced by $(F_1 + F_p)$ where F_p is the preload force. The virtual work derivation would also include the effects of F_p at the location of F_2. Doing his results in a slightly different expression for F_1 given by

$$F_1 = \frac{F_{out}\left(\cos\frac{\theta_j}{2} - \cos\theta_r + \frac{L_j}{r_1}\right) - 2F_p r_1 \cos\theta_r \sin\frac{\theta_j}{2}}{\sin\left(\theta_r + \frac{\theta_j}{2}\right)} \tag{3.13}$$

This new expression for F_1 which includes a preload force on the system shows two interesting behaviors that occur. First, by including a preload force on both cables, the required input force is reduced when θ_j is between 0 and 90°, but is increased when θ_j is between 0 and $-90°$. Second, for $\theta_r = 90°$ the preload force has no effect on the required input force and Eq. 3.13 becomes equivalent to Eq. 3.12.

3.2.4 Example Design

To demonstrate the use of these equations of motion, consider a design where the desired jaw rotation is ±90° with a jaw length of 6.25 mm and a desired output force of 2 N. Assume that there is not a preload force in the cables. To achieve this motion θ_r must be at least 45°. To provide reasonable structural support at the extremes of motion, we will choose $\theta_r = 60°$. In this example, we will design the instrument to fit within a 3 mm circle so that it can be attached to a 3 mm shaft. To do this, we can assume that the base of Split CORE joint is square. Therefore, one side of the square is equal to $2r_1 \sin\theta_r$. The diagonal of the square will be equal to the diameter of the desired shaft size (3 mm). Using this information r_1 is calculated as follows:

$$(3\ mm)^2 = 2\,(2r_1 \sin\theta_r)^2 \tag{3.14}$$

$$r_1 = \sqrt{\frac{9}{8\sin^2\theta_r}} \tag{3.15}$$

$$r_1 = 1.23\ mm \tag{3.16}$$

The distance from the upper segment to the point of force application (d_f) must also be determined in this design. One option that will be used here is to define this distance as the point where the force would be applied if θ_r were equal to 90°. Doing this gives the design the same mechanical advantage as a traditional CORE mechanism, but its overall height is reduced because the actual profile is defined by $\theta_r = 60^\circ$. Therefore, calculating d_f is done using the following relation:

$$d_f = r_1 - r_1 \sin\theta_r \tag{3.17}$$

$$d_f = 0.165\ mm \tag{3.18}$$

With these values the input force, F_1, can be determined for any jaw rotation using Eq. 3.12. In this calculation the value of $\theta_r = 90^\circ$ will be used because that defines the location of force input. For other calculations such as segment height and range of motion, $\theta_r = 60^\circ$ would be used. Figure 3.4 shows the required input force for a range of θ_j from -90° to 90°. This plot shows that the required force is symmetric about $\theta_j = 0$ and ranges between approximately 12 and 16 N. The locations of greatest force are at the extremes of motion. This is to be expected because it is where the moment arm of force application is minimized. A plot of the mechanical advantage, shown in Fig. 3.5, also illustrates this concept where mechanical advantage is maximum at $\theta_j = 0$.

In addition to the force requirements, mechanical advantage also gives some insight into the control and precision of the instrument. Mechanical advantage can be used to describe the relationship between input displacement and output displacement. In this particular design, the input displacement is the amount of motion in the actuation cable. The output displacement cor-

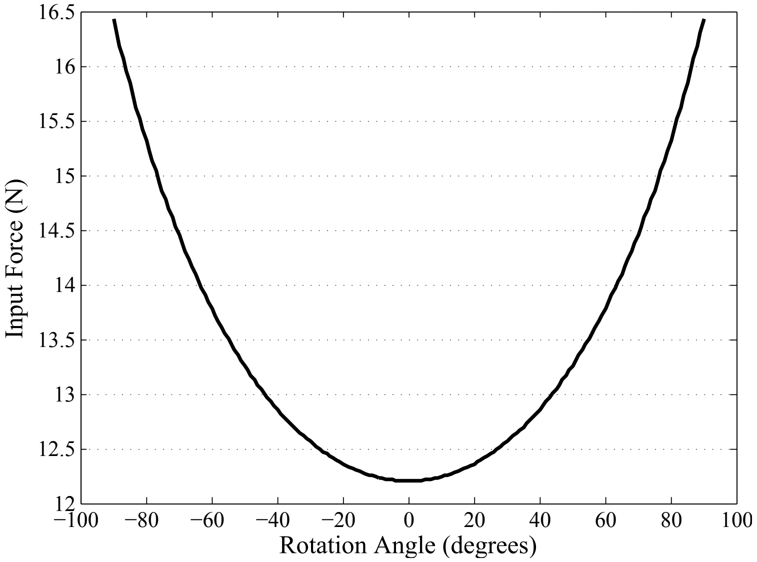

Figure 3.4: Plot showing the required input force for a Split CORE mechanism with ±90° of rotation and an output force of 2 N.

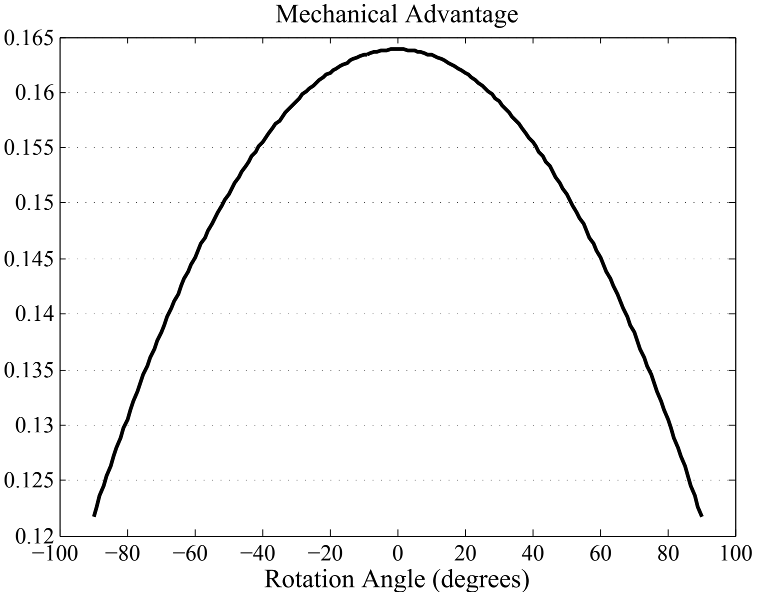

Figure 3.5: The mechanical advantage of an example design for a range of rotation angles from -90 to 90°.

responds to the displacement of the tip of the jaw where F_{out} is positioned (see Fig. 3.3). For the example design given, this means that when $\theta_j = 0$ (where M.A. = 0.164) a 1 mm displacement of the actuation cable would result in an output displacement of approximately 6.10 mm. This is based on the following relationship:

$$MA = \frac{input\ displacement}{output\ displacement} \tag{3.19}$$

There are a few different ways to maximize precision and control of the instrument tip. One way is to increase the mechanical advantage of the system. This can be done by increasing the radius of curvature in the upper and lower segments (r_1). Another way to accomplish improved control is to reduce the diameter of the spool which is used to actuate the cable. With a smaller diameter spool, a given rotational input will result in a smaller cable displacement than would occur with the same rotational input on a larger spool. This method does not change the required input force (or mechanical advantage) but it does improve the control of the motion at the jaw tip.

3.3 Stress Analysis

The critical stresses experienced by the Split CORE mechanism can be determined using Hertzian Contact Stress Theory. Contact stress theory is used to model the interfacial stresses between two mating solids. In the case of two circular surfaces, the area of contact forms a rectangle of width $2b$ and length l. The length, l, is simply the total length of the flat regions carrying the compressive loads (refer to Fig. 3.2). Using the parameters shown in Fig. 3.3 and using the theory in [52], the half width of the stress area, b, is given by the following equation:

$$b = \sqrt{\frac{4r_1F\left(1-\nu^2\right)}{\pi l E}} \tag{3.20}$$

where F is the input force F_1 or F_2, depending on which case is being considered, ν is Poisson's ratio, and E is the modulus of elasticity for the material being used. Equation 3.20 assumes that the radius of curvature for upper and lower segments are equal and that both are of the same material.

The contact area creates an elliptical pressure distribution with its maximum at the center. The distribution is shown in Fig. 3.6. The maximum pressure is defined as

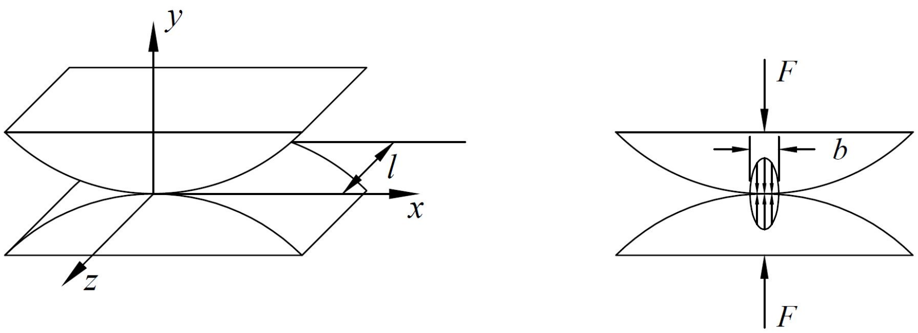

Figure 3.6: Geometry depicting the parameters used to determine the stress states caused by contact between the upper and lower segments of the Split CORE design.

$$P_{max} = \frac{2F}{\pi b l} \tag{3.21}$$

Subsequently, the stress states along each of the three axes can be expressed in terms of the distance away from the point of contact, or the depth into the material. This depth is denoted as y, as it corresponds to the y axis. These expressions are given by the following three equations.

$$\sigma_x = -P_{max}\left(\frac{1+2\left(\frac{y}{b}\right)^2}{\sqrt{1+\left(\frac{y}{b}\right)^2}} - \left|\frac{y}{b}\right|\right) \tag{3.22}$$

$$\sigma_y = \frac{-P_{max}}{\sqrt{1+\left(\frac{y}{b}\right)^2}} \tag{3.23}$$

$$\sigma_z = -2\nu P_{max}\left(\sqrt{1+\left(\frac{y}{b}\right)^2} + \left|\frac{y}{b}\right|\right) \tag{3.24}$$

3.3.1 Example Design

The parameters used in the previous example will be used here to determine the stress states at the contact point of the mechanism. For this design, we will say that the material being used is titanium (Ti-6Al-4V) with an elastic modulus of 114 GPa, compressive yield strength of 1070 Mpa, and Poisson's ratio of 0.34. We will also assume that the non-geared portion of the contact surface (see Fig. 3.2) is one third of the total length of the joint, where the length of the

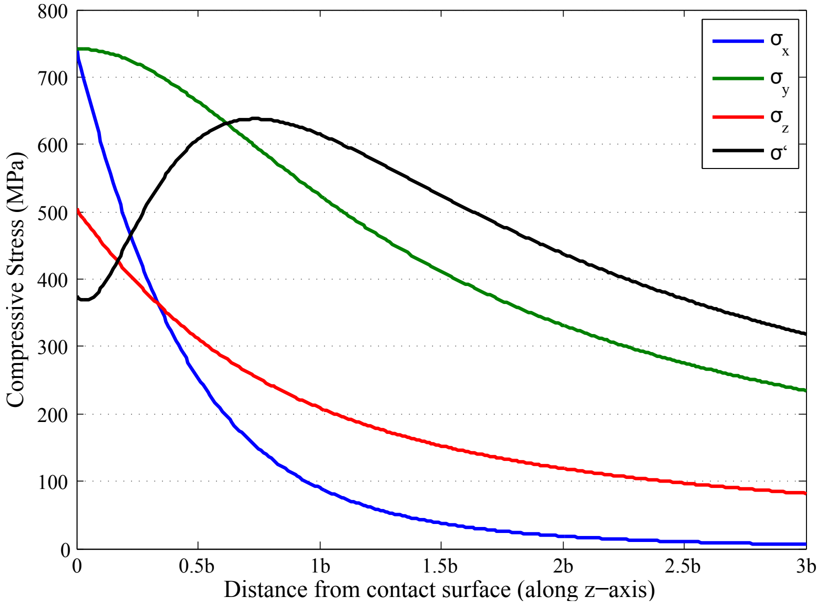

Figure 3.7: Plot showing the stress states at the contact point when the example design is in the vertical position ($\theta_j = 0$).

joint is equal to $2r_1$, or 2.12 mm, so that it fits on a 3 mm instrument shaft. The remaining portion of the surfaces is comprised of gear teeth which only transmit loads associated with motion. From this information the length, l, is calculated to be approximately 0.7 mm and the contact width, b is calculated using Eq. 3.20. These calculations are based on the position at which θ_j is zero, which corresponds to $F_1 = 12.2$ N. However, this same approach can be used to determine the contact stresses at any angle of rotation.

$$b = \sqrt{\frac{4\,(0.00123)\,(12.2)\,(1-0.34^2)}{\pi\,(0.0007)\,(114\times10^9)}} \tag{3.25}$$

$$b = 0.015\ mm \tag{3.26}$$

These values are substituted into Eq. 3.21 to calculate the contact pressure which gives a value of $P_{max} = 742$ MPa. Lastly, these values are substituted into Eqs. 3.22-3.24 to determine each of the stress states. These stresses are shown in Fig. 3.7. The maximum stress in each of the three directions occurs at the outer surface where contact is made. The maximum stresses for σ_x, σ_y, and σ_z at this location are 742 MPa, 742 MPa, and 504 Mpa, respectively. This results in a

Figure 3.8: 3D printed Split CORE Grips attached to a 3.4 mm diameter instrument shaft. 5 and 8 mm diameter instruments shown for comparison.

maximum Von Mises stress of $\sigma' = 638$ MPa. The location of the maximum Von Mises stress is approximately 0.011 mm from the contact surface ($z \approx 0.74b$). This gives a minimum safety factor of 1.68.

3.4 Prototyping and Testing

Several prototypes of the Split CORE mechanism were created on a 10:1 scale to test functionality and make design improvements on the Split CORE Grips. Later, prototypes were created on a 1:1 scale and retrofitted onto da Vinci instrument shafts. The prototype shown in Fig. 3.8 is a 3D-printed polymer model. Another prototype was made using stacked layers of lithographically patterned carbon nanotube composite material. This fabrication method is discussed further in Chapter 6.

These prototypes verified the expected performance of the Split CORE Grips, and also revealed important challenges that should be addressed to improve upon the design.

3.5 Conclusions

The motion of the Split CORE gripper mechanism is straightforward and predictable. Given a desired rotation angle and output force, the required input forces can be calculated. Also, because the jaw segments roll, rather than slide, along the surface of the lower segment the effects of friction are minimal. The critical stresses in the system are due to compressive contact and occur at rolling contact between upper and lower segments. These stress can also be predicted for a particular rotation angle and output force.

There are several advantages to this design including the fact that friction forces are nearly non-existent and that the system consists of only three parts with relatively simple geometries. The design includes some functional trade-offs between range of motion, force input requirements and overall instrument size. This allows the mechanism to be tailored to best address the needs of a particular situation.

CHAPTER 4. DESIGN ANALYSIS OF AN INVERTED FLEXURE MECHANISM

4.1 Introduction

The inverted flexure design consists of two jaws, each of which use a single compliant segment to combine gripping motion and wrist motion. The flexures are “inverted” so that the loads on the flexure are in tension and bending rather than compression, thus avoiding buckling. Compliant mechanisms offer many advantages compared to a rigid-body mechanism. One advantage is that there is little friction because there are no mating parts moving relative to one another. In the inverted flexure design, the two jaw parts will move relative to one another but they do not necessarily need to be in contact with one another.

Another advantage to using a compliant segment in the inverted flexure design is the reduction in number of parts. A rigid-body design with similar motion would require additional parts to create a pin joint where the jaw body can attach. Instead, the flexure takes the place of a pin joint and can be integrated directly into the jaw body.

Figure 4.1 illustrates the basic geometry of the Inverted Flexure mechanism attached to the instrument shaft and actuation cables, which are controlled by the robotic controls interface at the base of the instrument. The derivations for kinematic behavior, mechanical advantage, and stress are described and are based on this geometry.

4.2 Kinematics

The Inverted Flexure design relies on a thin flexure that is inverted such that it is in tension. To understand the motion of the flexure, and subsequently the rigid portion of the gripper, the pseudo-rigid-body model can be used [53]. The thin flexure can be modeled as a small-length flexural pivot, which means that the motion can be approximated as that of a pin joint with a torsional spring. The location of the pivot is referred to as the characteristic pivot and is half the

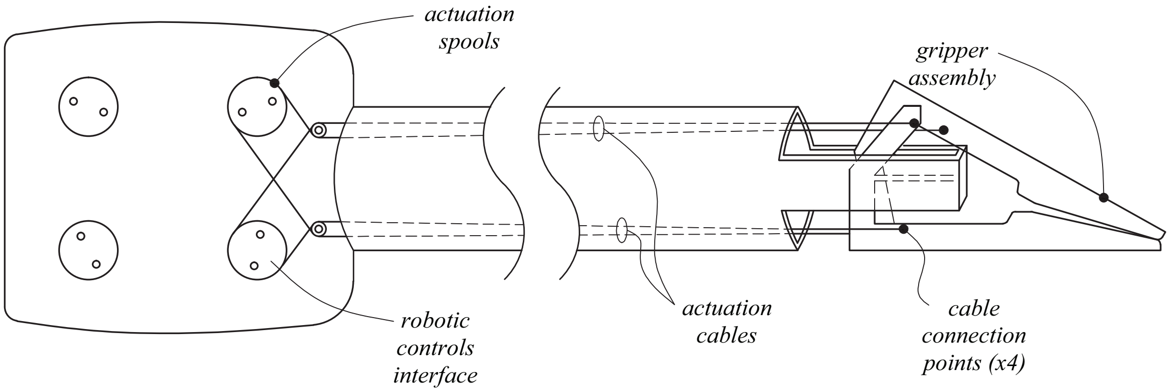

Figure 4.1: Diagram of the Inverted Flexure design attached to the instrument shaft and actuation controls (features not to scale).

distance of the flexure length from its fixed point. Figure 4.2 shows the actual model and the pseudo-rigid-body representation.

The points of force application are illustrated in Fig. 4.2c. In this design, the forces are applied at the same level as the characteristic pivot (in the undeflected position). Assuming that the two cables are fixed to the same actuating spool (Fig. 4.1) at the base of the instrument, this ensures that the cables do not stretch or become slack. However, if the points of force application are located below the characteristic pivot, the cables will be required to stretch as the mechanism deflects to positions other than the undeflected position. This would cause stiffening of the flexure and would increase the required input forces. On the other hand, if the points of force application are located anywhere above the characteristic pivot, the cables become slack as the mechanism moves to any position other than the undeflected position. This would result in poor control of the mechanism.

To ensure a useful wrist and gripper design, the jaws should close flat upon each other throughout the entire range of motion. In some cases, it may be acceptable and even useful for the jaw tips to meet slightly ahead of the base of the jaws, as shown in Fig. 4.3. However, it is undesirable for the base of the jaws to meet prior to the tips meeting. Equations of motion to ensure that the jaws meet flat along the entire surface are developed here. Once these are developed, small modifications can be made to allow the second case where the jaw tips come in contact before the rest of the jaw surface.

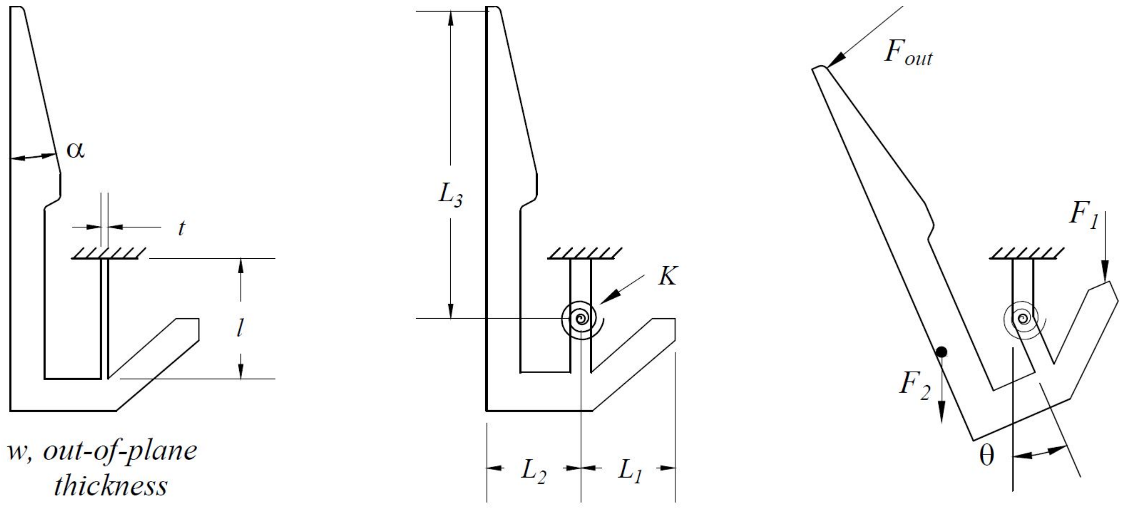

(a) (b) (c)

Figure 4.2: Diagrams of the compliant and pseudo-rigid-body models of the Inverted Flexure wrist and gripper design.

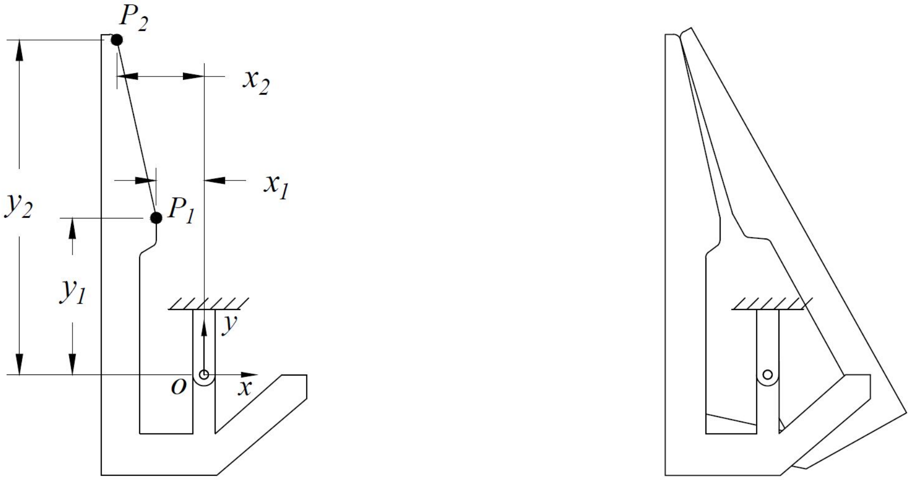

(a) (b)

Figure 4.3: (a) Diagram showing P_1 and P_2 used to ensure that the jaws close flat upon each other. (b) Depicts the case where the jaws meet first at the tips.

Three key points are identified in Fig. 4.3—the origin, O, and two points on the jaw surface, P_1 and P_2. One method to ensure the desired motion is to constrain these three points to be collinear. Based on the pseudo-rigid body model, the jaw bodies will pivot about the characteristic pivot, which is the same location as the origin in Fig. 4.3. Because the two jaw bodies both pivot about this common point, the requirement of collinearity will ensure that the surfaces of the jaws always meet.

Vectors from the origin can be used to define points P_1 and P_2. For the undeflected position, these vectors are defined as:

$$\mathbf{P_1} = (-x_1)\hat{\mathbf{i}} + (y_1)\hat{\mathbf{j}} \tag{4.1}$$

$$\begin{aligned} \mathbf{P_2} &= \mathbf{P_1} + \left[-(x_2 - x_1)\hat{\mathbf{i}} + (y_2 - y_1)\hat{\mathbf{j}}\right] && (4.2) \\ &= (-x_2)\hat{\mathbf{i}} + (y_2)\hat{\mathbf{j}} && (4.3) \end{aligned}$$

With the assumption of collinearity, $\mathbf{P_2}$ can be defined as $\mathbf{P_1}$ multiplied by a scalar, c, as in:

$$\begin{aligned} \mathbf{P_2} &= c\mathbf{P_1} && (4.4) \\ (-x_2)\hat{\mathbf{i}} + (y_2)\hat{\mathbf{j}} &= c\left[(-x_1)\hat{\mathbf{i}} + (y_1)\hat{\mathbf{j}}\right] && (4.5) \end{aligned}$$

Decomposing Eq. 4.5 into its $\hat{\mathbf{i}}$ and $\hat{\mathbf{j}}$ components yields the following constraints.

$$\begin{aligned} -x_2 &= -cx_1 && (4.6) \\ y_2 &= cy_1 && (4.7) \end{aligned}$$

Substituting Eq. 4.6 into Eq. 4.7 will yield an equation which, if satisfied, ensures that the flat faces of the jaws meet flush at any given angle of motion (within the bounds that will be discussed later). This equation is given as:

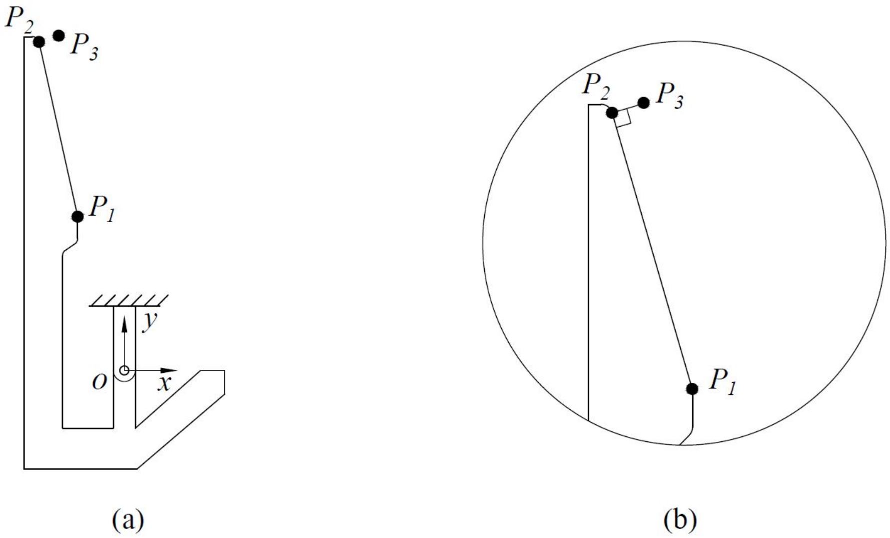

Figure 4.4: Points used to define the geometry of the jaw to ensure proper mating.

$$\frac{x_1}{y_1} = \frac{x_2}{y_2} \tag{4.8}$$

For the case where it may be desirable to design the jaws to come in contact first at their tips, a third point, P_3, can be defined at some point near P_2 but slightly offset from the surface of the jaw, as in Fig. 4.4. Two more vectors can be used to define this new point—a vector from the origin to P_3 ($\mathbf{P_3}$) and a vector from P_2 to P_3 ($\mathbf{P_{2,3}}$).

For simplicity, $\mathbf{P_{2,3}}$ can be defined orthogonal to $\mathbf{P_2}$ as in Eqs. 4.9 and 4.10. Furthermore, the offset distance, or magnitude of $\mathbf{P_{2,3}}$, can be defined as a fraction of the length of the jaw. For example, if d_{jaw} is used as a scalar, Eq. 4.11 can be used to determine the offset distance.

$$\mathbf{P_{2,3}} \perp \mathbf{P_2} \tag{4.9}$$

$$\mathbf{P_2} \cdot \mathbf{P_{2,3}} = 0 \tag{4.10}$$

$$\|\mathbf{P_{2,3}}\| = d_{jaw} \|\mathbf{P_2} - \mathbf{P_1}\| \tag{4.11}$$

To solve for $\mathbf{P_{2,3}}$, Eq. 4.10 can be expanded as shown in Eq. 4.12 where x_{23} and y_{23} represent the $\hat{\mathbf{i}}$ and $\hat{\mathbf{j}}$ components of $\mathbf{P_{2,3}}$, respectively. This provides one equation, but two unknown values. The expanded form of Eq. 4.11 can serve as a second equation and is shown in Eq. 4.13.

$$\left[(-x_2)\hat{\mathbf{i}} + (y_2)\hat{\mathbf{j}}\right] \cdot \left[x_{23}\hat{\mathbf{i}} + y_{23}\hat{\mathbf{j}}\right] = 0 \tag{4.12}$$

$$\sqrt{(x_{23})^2 + (y_{23})^2} = d_{jaw}\sqrt{(x_1 - x_2)^2 + (y_2 - y_1)^2} \tag{4.13}$$

These two equations can be solved simultaneously for x_{23} and y_{23} which results in the following equations:

$$x_{23} = \frac{y_2}{x_1}\left[\frac{{d_{jaw}}^2}{\left(\frac{y_2}{x_1}\right)^2 + 1}\left[(x_1 - x_2)^2 + (y_2 - y_1)^2\right]\right]^{1/2} \tag{4.14}$$

$$y_{23} = \left[\frac{{d_{jaw}}^2}{\left(\frac{y_2}{x_1}\right)^2 + 1}\left[(x_1 - x_2)^2 + (y_2 - y_1)^2\right]\right]^{1/2} \tag{4.15}$$

Once these points are calculated, the jaw can be designed to extend from P_1 to P_3 rather than from P_1 to P_2. The derivation of these equations is based on the assumption that the small length flexural pivots of the two jaws act purely as a pin joint. While this model is a relatively good approximation, there will be a small degree of motion that does not follow this behavior. This will be exhibited by finite element modeling and physical testing of prototypes.

4.2.1 Comparison of PRB and FE models

A comparison between the pseudo-rigid body model and finite element model can be used to verify the accuracy of kinematic motion predicted by hand calculations. The outline of the mechanism shown in Fig. 4.5 shows four points on the body of the mechanism: one point at the bottom of the flexure, one point at each of the input force locations (see Fig. 4.2), and one point at the tip of the jaw. The plot shown in Fig. 4.5 shows the motion paths that each point follows as they move from $\theta = 0$ to $\theta = -45$ degrees. The pseudo-rigid-body and finite element models

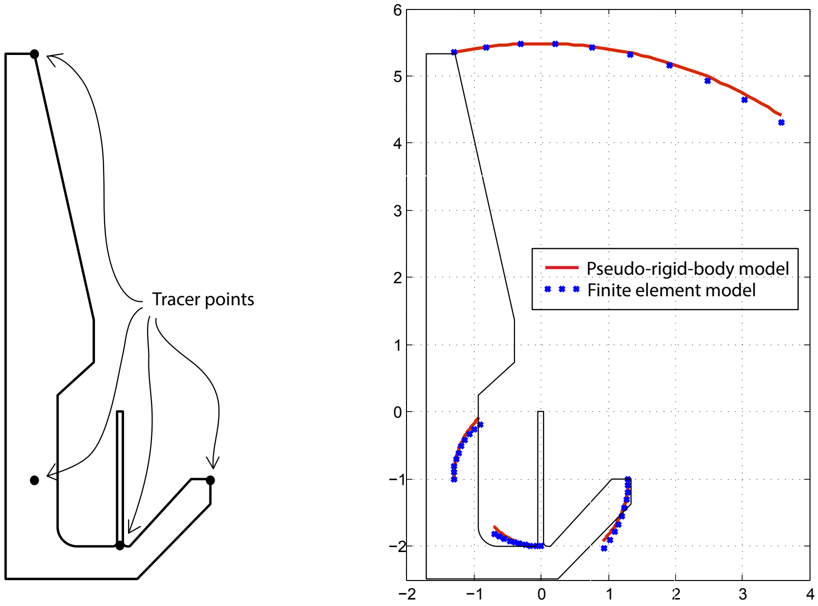

Figure 4.5: Points used to trace motion paths predicted by pseudo-rigid-body and finite element models (left). Motion paths predicted by PRB and FE models for motion from $\theta = 0$ to $\theta = -45$ degrees (right). Reference grid is in millimeters.

agree closely with one another. There is some deviation as θ increases, however the error is small indicating that modeling the flexure as a small-length flexural pivot is a reliable method for predicting kinematic behavior.

4.3 Mechanical Advantage

The mechanical advantage in this design is defined as the ratio of the force output, F_{out}, at the jaw tip to the force input at the ends of the input arm. Two input forces are defined—F_1 and F_2—and they vary in magnitude depending on the desired direction of actuation. However, an assumption can be made regarding the relationship between F_1 and F_2. If the actuating cables attached at the points of F_1 and F_2 are connected to a common spool, then as a force is applied to one cable, the force in the opposite cable goes to zero. For example, under this assumption if F_1 equals 2 N then F_2 is zero. This assumption will be used in the derivation of mechanical advantage. From this point on, the case where $F_1 \geq 0$ and $F_2 = 0$ will be used to help illustrate the use of the derivations. Thus, F_{in} is equal to F_1. However, the derivations are also suited for the case where $F_2 \geq 0$ and $F_1 = 0$.

Mechanical advantage can be calculated using the principle of virtual work. Using this method will provide an equation for F_1 as a function of output force, F_{out}, and rotation angle, θ. Once F_1 is calculated, the mechanical advantage is given by the ratio of F_{out} to F_1.

The first step in calculating the virtual work in the system is choosing a generalized coordinate. The most convenient variable in this case is the rotation angle, θ. Next, each of the applied forces are written in vector form. These consist of F_1 and F_{out}. In the derivations that follow, the rotation angle, θ, is defined to be positive in the counter-clockwise direction and α is used to denote the jaw angle (see Fig. 4.2c).

$$\mathbf{F_1} = -F_1\hat{\mathbf{j}} \tag{4.16}$$

$$\mathbf{F_{out}} = F_{out}\left(-\cos(\theta+\alpha)\hat{\mathbf{i}} - \sin(\theta+\alpha)\hat{\mathbf{j}}\right) \tag{4.17}$$

Next, position vectors are written from the origin to the placement of the applied forces. Like in Fig. 4.4a, the origin is located at the characteristic pivot which is half the distance of the flexure length from the fixed point.

$$\mathbf{Z_1} = L_1\cos(\theta)\hat{\mathbf{i}} + L_1\sin(\theta)\hat{\mathbf{j}} \tag{4.18}$$

$$\mathbf{Z_{out}} = (-L_2\cos\theta - L_3\sin\theta)\hat{\mathbf{i}} + (-L_2\sin\theta + L_3\cos\theta)\hat{\mathbf{j}} \tag{4.19}$$

The virtual displacement can now be calculated by differentiating the position vectors with respect to the generalized coordinate.

$$\delta\mathbf{Z_1} = \left(-L_1\sin\theta\hat{\mathbf{i}} + L_1\cos\theta\hat{\mathbf{j}}\right)\delta\theta \tag{4.20}$$

$$\delta\mathbf{Z_{out}} = \left[(L_2\sin\theta - L_3\cos\theta)\hat{\mathbf{i}} + (-L_2\cos\theta - L_3\sin\theta)\hat{\mathbf{j}}\right]\delta\theta \tag{4.21}$$

The virtual work, δW, is calculated by taking the dot product of the force vectors from Eqs. 4.16 and 4.17 and the virtual displacement vectors from Eqs. 4.20 and 4.21.

$$\delta W_1 = (-F_1L_1\cos\theta)\,\delta\theta \tag{4.22}$$

$$\begin{aligned}\delta W_{out} &= F_{out}L_2\left[\cos(\theta)\sin(\theta+\alpha)-\sin(\theta)\cos(\theta+\alpha)\right]\delta\theta \\ &+ F_{out}L_3\left[\cos(\theta)\cos(\theta+\alpha)+\sin(\theta)\sin(\theta+\alpha)\right]\delta\theta\end{aligned} \tag{4.23}$$

The virtual work due to the compliance of the flexure must also be accounted for. This is done by first determining the potential energy of the torsional spring that is used in the pseudo-rigid-body model.

$$V = \frac{1}{2}K\left(\theta-\theta_o\right)^2 \tag{4.24}$$

In this equation θ_o is zero and the torsional spring constant, K, is defined as EI/l. Next, the virtual work is calculated by differentiating the potential energy with respect to the generalized coordinate and multiplying by $-\delta\theta$.

$$\delta W_{spring} = -K\theta\ \delta\theta \tag{4.25}$$

The total virtual work in the system is calculated by summing each component of virtual work from Eqs. 4.22, 4.23, and 4.25. Lastly, once the total virtual work is calculated, the principle of virtual work states that if the system is in equilibrium then the virtual work is equal to zero. This can be used to determine F_1.

$$\begin{aligned}\delta W &= \left(-F_1L_1\cos\theta\right)\delta\theta + F_{out}L_2\left[\cos(\theta)\sin(\theta+\alpha)-\sin(\theta)\cos(\theta+\alpha)\right]\delta\theta \\ &+ F_{out}L_3\left[\cos(\theta)\cos(\theta+\alpha)+\sin(\theta)\sin(\theta+\alpha)\right]\delta\theta - \frac{EI\theta}{l}\delta\theta \\ &= 0\end{aligned} \tag{4.26}$$

$$F_1 = \frac{F_{out}\left(L_2\sin\alpha + L_3\cos\alpha\right) - \frac{EI\theta}{l}}{L_1\cos\theta} \tag{4.27}$$

4.3.1 Including a Preload Force

It may be desirable to apply a certain amount of preload force to the points of force application (Fig. 4.2c). This would reduce any effects of backlash that may occur and would ensure higher levels of control over the motion of the mechanism. If an equal preload force is applied

Table 4.1: Example design parameters

Parameter	Value	Parameter	Value
L_1	1.30 mm	l	2.00 mm
L_2	1.30 mm	w	0.50 mm
L_3	6.35 mm	t	0.080 mm
α	12.5°		

to both sides of the mechanism (i.e. equal preload in both actuation cables) then the changes to the previous derivations are relatively simple. The input force term, F_1, in Eq. 4.26 is replaced by $(F_1 + F_p)$ where F_p is the preload force. The virtual work calculations would also need to account for the force at the point of F_2 where $F_2 = F_p$. This results in a slightly different expression for F_1 given by

$$F_1 = \frac{F_{out}\left(L_2 \sin\alpha + L_3 \cos\alpha\right) - \frac{EI\theta}{l} + \left(L_2 - L_1\right) F_p \cos\theta}{L_1 \cos\theta} \tag{4.28}$$

Further, this new equation for F_1 indicates that if L_1 and L_2 are equal, the preload force has no effect on required input force or mechanical advantage. In this case, Eqs. 4.27 and 4.28 are equivalent.

4.3.2 Example Design

The input force can be calculated for a set of desired parameters to illustrate the use of these equations. In this example the input force values will be calculated for a desired output force of 0.5 N over a range of $\theta = 0$ to $\theta = 45$ degrees. The material used in this example will be metallic glass because its material properties make it well suited for compliant designs [54]. The modulus of elasticity, E, is 95 GPa, and the yield strength, S_y, is 1800 MPa.

The parameters associated with jaw geometry are defined in Table 14.1. These parameters are chosen such that the resulting mechanism would be approximately 3 mm in diameter. Using these parameters results in a range of values for mechanical advantage that starts at approximately 0.20 and gradually drops to just below 0.15 at 45° rotation. Figure 4.6 is a plot of the values of mechanical advantage for this range of motion.

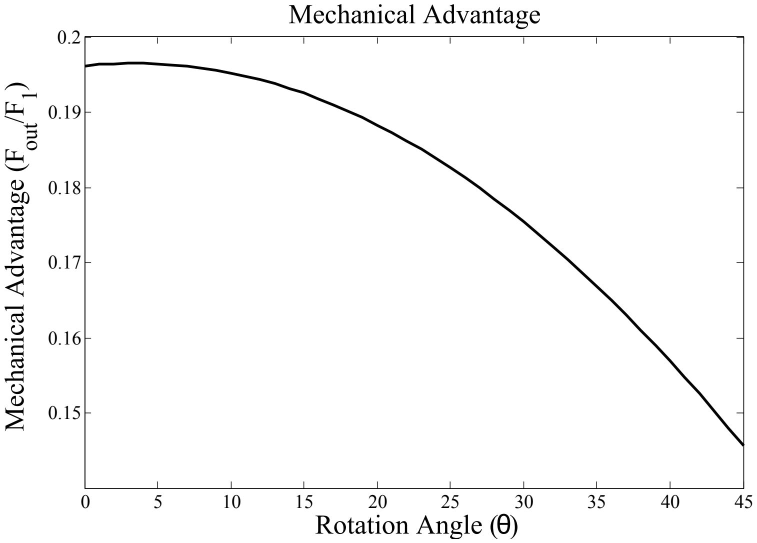

Figure 4.6: Mechanical Advantage for a range of 0 to 45 degrees for the sample design described.

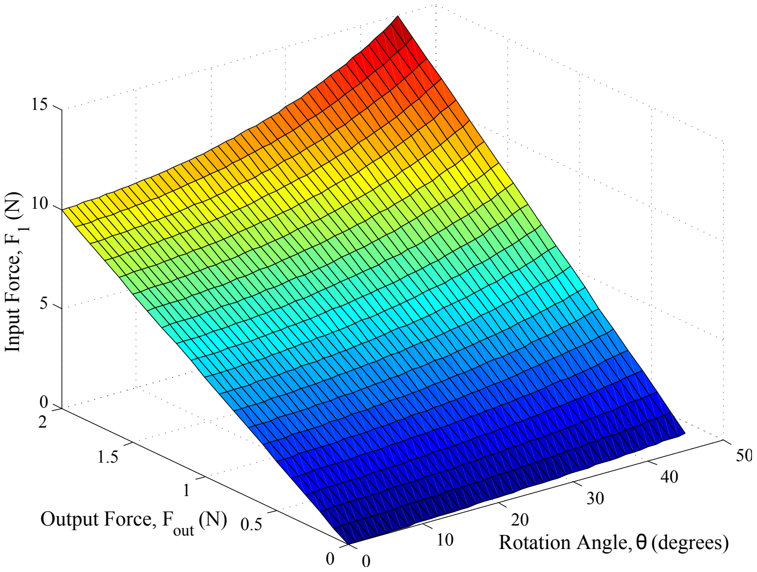

Figure 4.7: Required input force (F_1) calculated for a range of output force and rotation angle values using Eq. 4.27.

The required input force can be calculated for any given values of F_{out} and θ. Figure 4.7 shows a surface plot of the required input force for a range of output forces from 0 to 2.0 N and a range of rotation angles from 0 to 45°.

4.4 Stress Analysis

The largest stress within the system will occur in the small-length flexural pivot. The stress in the small-length flexural pivot is a combined result of bending and tension. The finite element model used to determine kinematic behavior previously can also be used to determine the magnitude and locations of the maximum stress in the beam. The finite element software package ANSYS was used to analyze the geometry shown in Fig. 4.5. The model consists of solid elements (element type SOLID185) and is based on the same dimensions used in the example to calculate input force (shown in Table 1). The top of the flexure is fixed from any lateral or rotational motion. To ensure that the output force (F_{out}) is always orthogonal to the jaw face, it is modeled as a pressure applied to a finite area at the end of the jaw. Lastly, the input force (F_1) is applied to the point shown in Fig. 4.2. It is calculated using Eq. 4.27 and is applied vertically downward.

4.4.1 Finite Element Analysis Results

As an example, Figure 4.8 shows the distribution of stress in the flexure at $\theta = -45$ degrees when the output force is 0.3 N. As these results show, the stresses in this particular design are quite significant. They are slightly beyond the yield strength of the metallic glass (1800 MPa), leaving no room for a safety factor. Some of the things that can be done to reduce these stresses include making the flexure thinner and/or longer, selecting a material with a higher strength-to-modulus ratio, or reducing the length of the jaw which would subsequently reduce the required input forces.

4.5 Conclusion

The Inverted Flexure mechanism relies on the compliance of a thin flexure that is arranged such that it is always in tension. This arrangement prevents the flexure from buckling and provides more predictable motion. The pseudo-rigid-body model can be used to predict the kinematic behavior of the Inverted Flexure mechanism. When modeling the mechanism as a small-length flexural pivot, the pseudo-rigid-body model agrees closely with the motion predicted by a finite element model.

The greatest stresses in the mechanism occur in the flexure. These stresses can be analyzed using finite element modeling where the output force is predetermined and the input force is

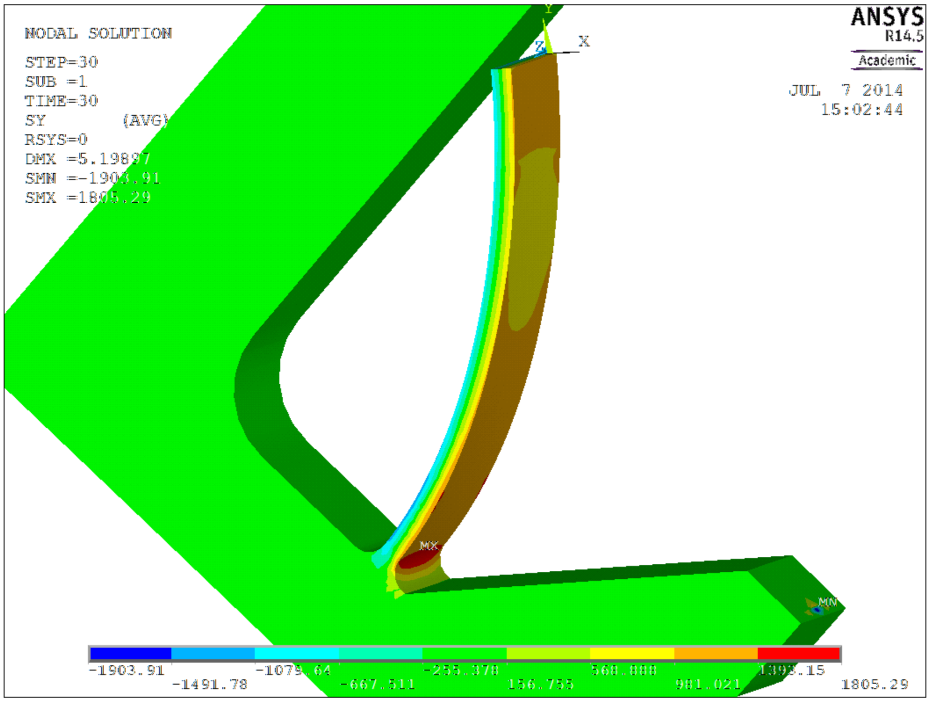

Figure 4.8: Finite element model showing the stresses in the flexure when an output force of 0.3 N is applied at an angle of 45°. Units are in MPa.

calculated based on the principle of virtual work. For the example design discussed, the stresses exceeded the yield strength of the material as motion went beyond 45° and force output exceeded approximately 0.3 N. Because these results are undesirable, two possible strategies could be used to make use of this design:

1. Recognize that the design has limitations in terms of range of motion and force output and ensure that it does not exceed these limitations, or
2. redesign the geometry and/or select a different material for the mechanism design.

In case 1 the mechanism could be limited to use in which the needed range of motion is less than ±45°. For example, in Chapter 1 several scenarios were described in which a 3 mm surgical instrument could potentially be employed. Among these, two stand out as scenarios where a small range of motion might achieve the desired functionality for the types of procedures that would be performed. In Fig. 4.9(a) the end effector is used at the bottom of a narrow cavity where motion is limited. In the second scenario, Fig. 4.9(b), the end effector is used at a blockage site within a lumen. Thus, the motion in this case is also limited to the area ahead of the instrument and not so much to the sides.

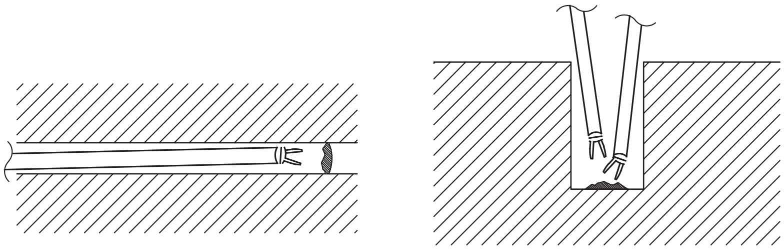

(a) (b)

Figure 4.9: Scenarios in which a surgical instrument potentially requires a reduced range of motion.

In case 2 there are a number of alterations that can be made to the design, or to the performance requirements of the mechanism to improve design feasibility. For example, the stress in the flexure can be reduced by making the flexure thinner. This would, in turn, increase the range of motion that can be achieved. Other ways to reduce the stress include selecting a material with a higher strength-to-modulus ratio, or by reducing the required output forces of the mechanism. However, there are also functional trade-offs that are associated with these possible design alterations. For example, while a thinner flexure reduces stress and increases the range of motion, the manufacturability of the flexure comes into question.

Overall, the design is quite simple with highly predictable motion, but the magnitude of the stresses is significant in some of the designs variations. Thus, the functional trade-offs should be considered in light of the desired performance characteristics to determine the ideal design for this mechanism.

CHAPTER 5. DESIGN AND FABRICATION OF MILLIMETER-SCALE CROSSED-CYLINDER WRIST MECHANISM WITH TWO DEGREES OF FREEDOM

This chapter describes the design and fabrication of a 2-DOF wrist mechanism suitable for fabrication with maximum dimension on the order of 2-4 millimeters. The design is based on the idea of 2 half-cylinders in contact such that their axes lie orthogonal to each other. In that way, each cylinder can roll parallel to the other cylinders axis, giving 2 rotational degrees of freedom. To constrain the cylinders motion, unique gear teeth are designed that allow rolling motion in either orthogonal direction, but constrain all other motions. Contact can be guaranteed using a compressive force acting to push the cylinders together. We first demonstrate the design at centimeter scale using FDM 3D printing. Based on the smooth motion achieved, we fabricate a wrist with maximum dimension of 3 mm using layered sheets of carbon nanotube composite material. Each sheet is individually patterned using photolithography.

5.1 Introduction

Wrist mechanisms are commonly used in a wide variety of grasping, cutting, and manipulating operations. They allow control of the angle of a tool with respect to a mounting shaft. Typically, the wrist mechanism is placed at the end of the shaft, immediately before the tool (such as a cutter or grasper) to improve the dexterity of the tool. Figure 5.1 shows a surgical tool produced by Intuitive Surgical, Inc., which uses a 2-degree-of-freedom (2-DOF) wrist to mount the tool.

Several examples of wrist mechanisms have been presented in the literature. The DragonFlex tool used two sequentially-mounted rotational joints to achieve 2-DOF motion [6]. A similar wrist mechanism was described by Nai et al. [46]. A design based on planetary gearing, which decouples wrist and grasper motion, has also been demonstrated [42]. A design has also been presented in small scale (2.5 mm diameter) using compliant mechanisms and lithographic pat-

Figure 5.1: A surgical tool from Intuitive Surgical, Inc. mounted on a 2-DOF wrist. The tools shaft is approximately 8 mm in diameter.

terning [40]. However, the relatively complex design proved difficult to fabricate, and was only demonstrated in a 2X scale model.

Ideally, a wrist mechanism will allow large rotational motions (as large as ±90° is often desirable). In addition, the mechanism should operate with low swept volume to maximize maneuverability of the tool. Low friction and smooth motion are also important. Due to manufacturing constraints and the increased importance of friction at small scales, it has proven challenging to produce a wrist design with these characteristics appropriate for wrist size on the order of 2-4 mm.

This paper presents a design for a 2-DOF wrist mechanism capable of being manufactured with maximum dimensions on the order of 2-4 mm. The mechanism has minimal rubbing parts, resulting in low friction. We demonstrate fabrication at centimeter scale for testing using FDM 3D printing technology. We further demonstrate fabrication and assembly at the target size (3 mm diameter) using stacking of sheets of carbon nanotube composite material. Each sheet is lithographically patterned, and then assembled using a simple stacking procedure. The paper discusses further options for control of the mechanism.

5.2 Mechanism Design

The mechanism design is based on the concept of two cylinders in rolling contact with each other. A Compliant Rolling Contact Element (CORE) has previously been described [3], [47].

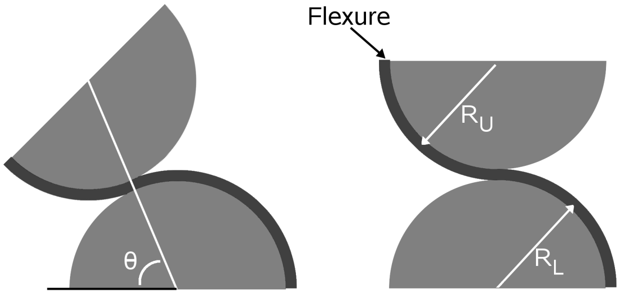

Figure 5.2: Two positions of a CORE mechanism, consisting of two half cylinders (shown end-on in this drawing) that can roll on one another. R_U and R_L are the radii of the two cylinders [3].

The concept of the CORE is shown in Figure 5.2. It uses two half cylinders (shown end-on in Figure 5.2) with axes aligned parallel to each other. The half cylinders roll on each other to produce primarily rotational motion, though there is also some translation. One or more thin flexures are then placed between the half cylinders, as shown, to constrain them from any motion other than rolling. As a result, the CORE has one degree of freedom.

In contrast to the CORE concept, the crossed-cylinder wrist mechanism is achieved by rotating one of the cylinders so that the axes of each half cylinder are orthogonal to each other. In this configuration, a flexure would impede motion in one of the desired directions, so gear teeth are substituted to prevent torsion and shear. A compressive force between the half-cylinders then ensures that the two pieces stay in contact with each other. A rendered model of the full mechanism is shown in Figure 5.3. As with the CORE mechanism, the two half cylinders experience only roll, and no sliding, with respect to each other. However, because the axes are orthogonal to each other, each half-cylinder rolls along a straight line on the surface of the other half cylinder, allowing 2 degrees of freedom (roll in either direction).

The gear teeth must be designed to function in two directions of roll. To accomplish this, each tooth has a cross-section of a rack tooth in the direction of the cylinders axis, and the cross-section of a normal spur gear tooth in the orthogonal direction, as shown in Figure 5.4. In this way,

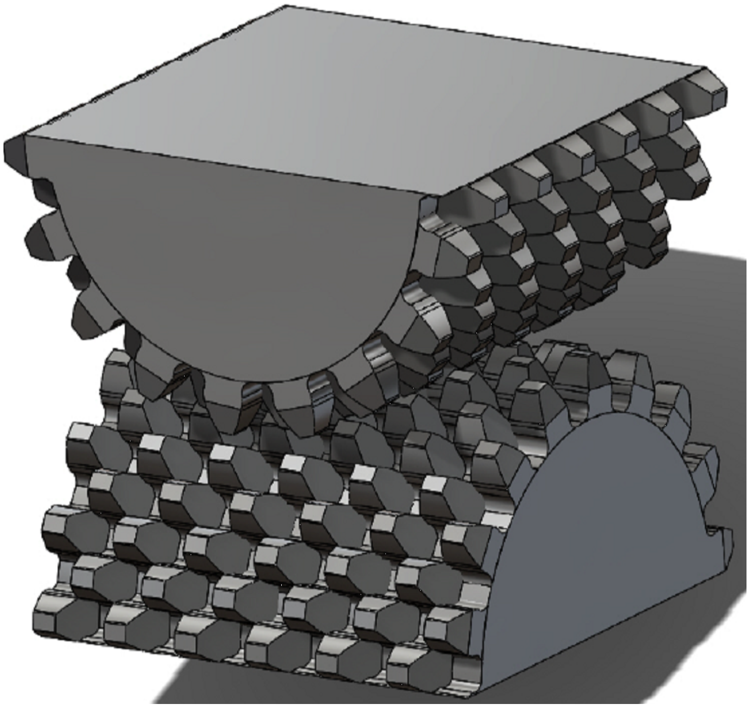

Figure 5.3: By rotating one half cylinder and adding gear teeth, the crossed-cylinder wrist mechanism is constrained to 2-DOF.

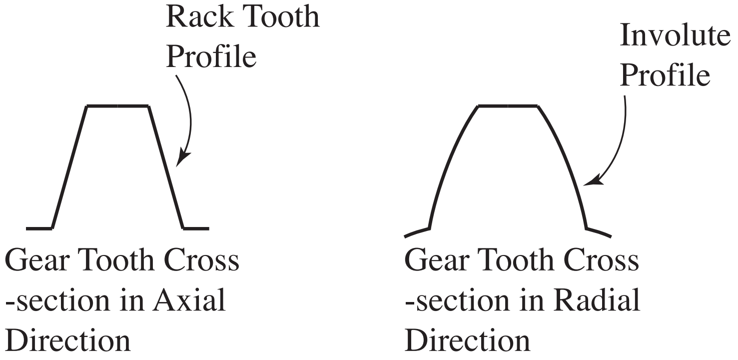

Figure 5.4: The gear teeth are shaped like a rack tooth in the axial direction, but have an involute spur gear profile in the radial direction.

each gear tooth can fit into a gap on the mating cylinder. By staggering (offsetting) a row of teeth, the motion is constrained while allowing both cylinders to be identical, reducing the number of unique parts. By comparison, some previous 3D gear tooth designs have required different tooth design on each part [55].

An important difference between the teeth in the crossed-cylinder mechanism and normal spur gear teeth is the load they are to carry. In normal spur gear teeth, the force always acts along the line of action, so that the most significant stresses in the tooth are often either shear stresses or bending stresses [52]. However, in the crossed-cylinder mechanism, the teeth must also support the compressive force acting to keep the two half cylinders in contact. Such stress could be analyzed using a finite element model.

5.3 Fabrication

To test the overall motion of the wrist, we fabricated a prototype at a relatively large scale using FDM 3D printing. The two geared half cylinders are shown separately in Figure 5.5(a). They are shown in three different positions in Figures 5.5(b)-5.5(d), with an angle of the top surface of approximately 0°, 45°, and 90° with respect to the horizontal.

The mechanism shown is designed with a pitch diameter of 3 cm, and 18 teeth per full circumference (9 teeth per half-circumference). The designed pressure angle is 20°, and it has 3% backlash. The addendum and dedendum were made using gear standards, so that the dedendum is slightly larger than the addendum. The mechanism was tested by placing the half cylinders together with their axes orthogonal to each other, as shown in Figure 5.5(b), and manually rotating the top half cylinder with respect to the bottom one. The motion was smooth without identifiable interference. The mechanism was able to rotate up to ±90° in both directions (along the bottom cylinders axis, and around the bottom cylinders circumference).

Based on the good performance achieved with the large-scale mechanism, we fabricated a wrist mechanism with maximum dimension (along the diagonal of the half-cylinders square) of 3 mm. The mechanism was fabricated from layers of carbon nanotube composite. The material consists of sheets of carbon nano-tube forests infiltrated by chemical vapor deposition with carbon. Fabrication details for this process are in Toone et al. [56]. Each sheet was lithographically patterned to produce a half-spur gear with alignment features, as shown in Fig. 5.6b. Thin spacer layers were also produced to give the right spacing between gear teeth. Because of the resolution used in the layering process (each tooth was produced using one layer), the sloped sides of the rack tooth profile were approximated using a rectangular profile. Each half cylinder was then assembled by stacking several sheets in the correct order on an electrical pin. The layers were held together

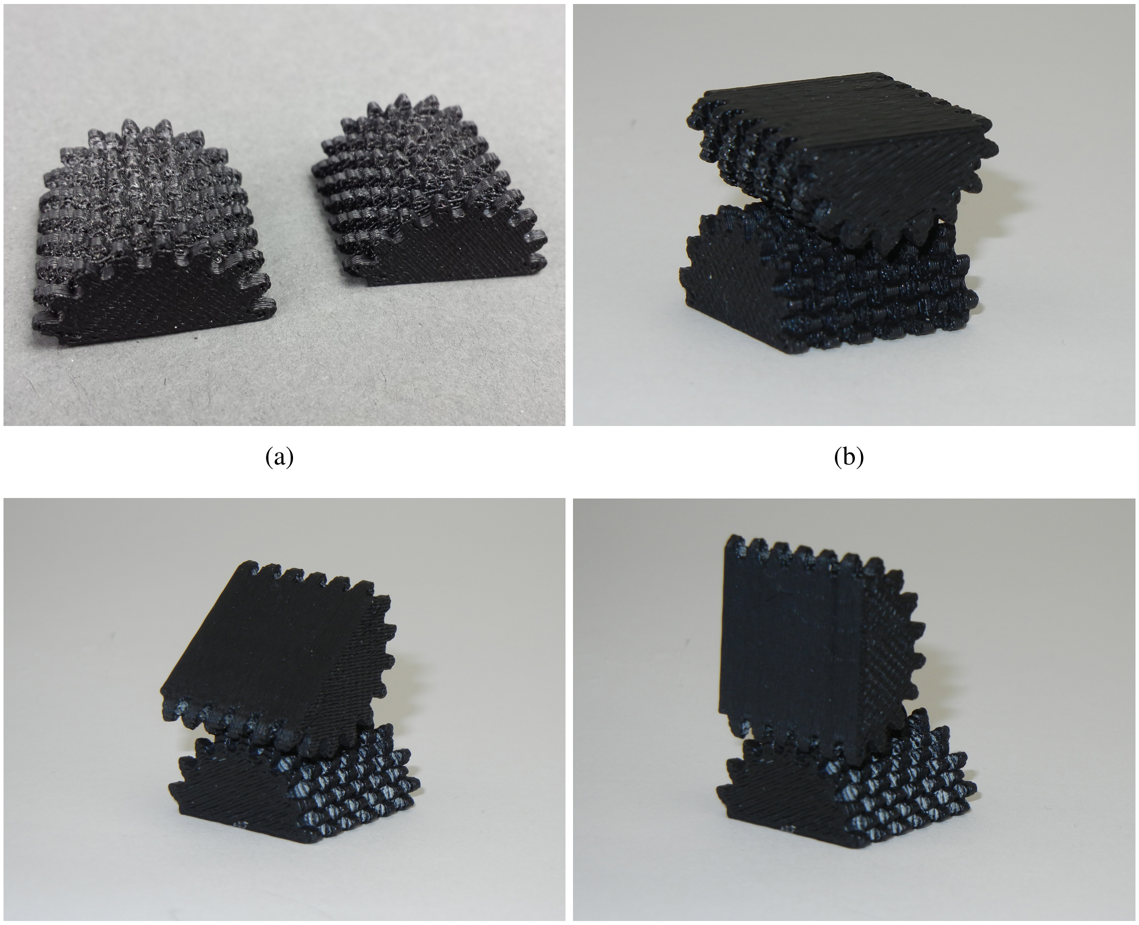

(a) (b) (c) (d)

Figure 5.5: Photographs of a prototype crossed-cylinders wrist fabricated using 3D printing.

using epoxy spread along the back surface of each half cylinder. Two views of an assembled half cylinder are shown in Fig. 5.6b and 5.6c, and the full wrist is shown in Fig. 5.6d.

The small-scale mechanism was designed with a pitch diameter of 2.03 mm and 18 teeth on the full circumference. The pressure angle was 25°, and the backlash was 5%. These small differences from the centimeter-scale prototype are not expected to cause significant performance changes. As with the centimeter-scale prototype, the dedendum of the gear teeth is 1.25 times the addendum.

The wrist is designed to be actuated by thin cables attached to the top half cylinder. Figure 5.7 shows the CNT prototype attached to an instrument shaft with cables arranged in a pull-pull

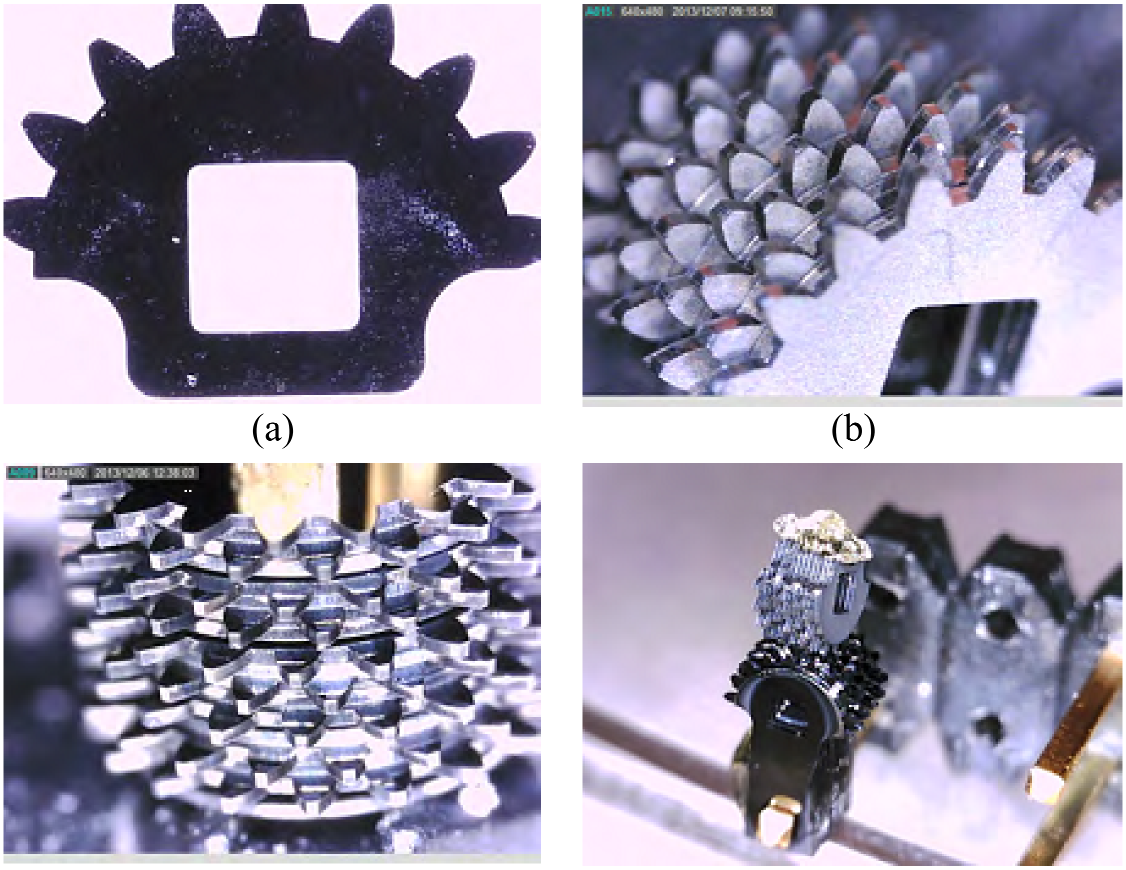
(a) (b)
(c) (d)

Figure 5.6: Micrographs of a millimeter-scale crossed-cylinder wrist mechanism fabricated by stacking carbon nanotube composite sheets. (a) A single layer, showing the gear teeth and alignment square for insertion of an electrical pin. (b) and (c) An assembled half cylinder. The reflections visible at the top of (c) are due to the smoothness of one side of the CNT sheet. (d) An assembled wrist mechanism, showing crossed cylinders mounted one on the other.

configuration to actuate both degrees of freedom. Further details and assessment of this fabrication method, including ways to improve stacking resolution and precision, are given in Chapter 6.

5.4 Conclusions

This paper presented a new design for a 2-DOF robotic wrist. The crossed-cylinder wrist mechanism experiences predominately rolling motion, minimizing friction during operation. It is also appropriate for manufacturing at small size scales. We have demonstrated a large-scale model fabricated using FDM 3D printing. The large-scale model validates the smooth motion achievable

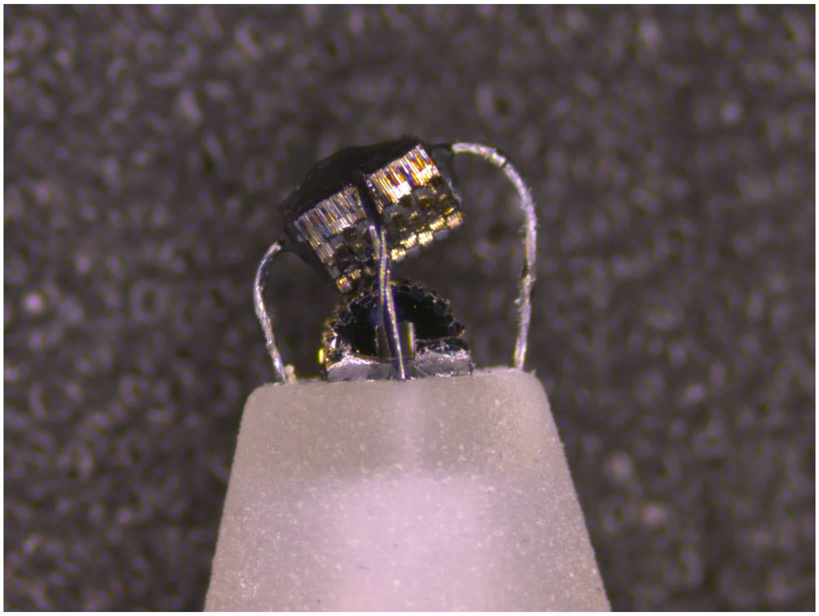

Figure 5.7: Crossed Cylinder wrist mechanism prototyped at 3 mm scale using carbon nanotube composite material.

using the wrist mechanism. It is capable of rotating ±90° in either of two directions (2-DOF). We have further demonstrated fabrication of the wrist mechanism at millimeter scale, with a maximum dimension of 3 mm. The small-scale wrist was fabricated by litho-graphically patterning sheets of carbon nanotube composite material, and then stacking the sheets to form two geared cylinders. The crossed-cylinder wrist design is expected to be used to improve dexterity and manipulation of small-scale tools, including cutters, graspers, and other robotic tools.

CHAPTER 6. FABRICATION PROCESS FOR MILLIMETER-SCALE ROBOTIC MECHANISMS USING LITHOGRAPHICALLY DEFINED CARBON NANOTUBE COMPOSITE STRUCTURES

6.1 Introduction

The use of robotic surgical instruments is ideal in minimally invasive surgical procedures because it allows precise control of the surgical instrument within small, confined areas. There is a drive to make these surgical instruments ever smaller to make surgery less invasive, improve patient outcomes [57, 58] and to open doors to procedures that may not be possible with current, larger instrumentation. However, as the surgical instruments become smaller, they become more difficult to fabricate.

Conventional machining techniques such as computer numerical control (CNC) milling or micro-electrical discharge machining (EDM) processes begin to reach their limits at the sub-millimeter feature size [59]. Even techniques such as metal injection molding, which are generally capable of producing complex geometries at the macro scale, are less suitable for sub-millimeter features because the molds themselves are typically produced through conventional machining techniques.

On the other end of the spectrum, micro and nano fabrication techniques, such as surface and bulk micromachining, are capable of producing extremely small features on the order of 100 nm [60]. However, these techniques are normally limited to planar geometries, making it difficult to adapt them to three-dimensional millimeter-scale mechanisms.

In an effort to bridge the gap between micro- and macro-scale mechanisms, several feasible techniques have been proposed as ways to fabricate robotics and other mechanisms on the millimeter scale. This size scale is commonly referred to as a meso-scale, and contains components with feature sizes as small as tens of micrometers, but whose overall dimensions may be several millimeters or even centimeters. Micromilling and laser ablation are two techniques demonstrated in [61]. The micromilling tools used are as small as 200 μm and are able to make precise cuts. The laser ablation method also achieves very small features but leaves a rougher surface finish. Solid freeform fabrication techniques are also rapidly emerging as methods for creating intricate geometries in a variety of engineering materials. Jabbari et al. [62] demonstrate the use of a sacrificial material to form biomimetic scaffolds using fused deposition modeling. The concept of layer-by-layer part manufacturing was presented in [63] in which foils were laser cut and adhered to adjacent layers to form a 3D object. Further development of this process has led to small part capabilities using photolithographic patterning and deposition [64]. Microfabrica, Inc. uses a technique in which a series of photo masks are used to define and join layers of a compliant electrical probe [65,66]. Another form of layered fabrication is used to create an autonomous, self-assembling robot that begins as a single flat sheet of material [67]. Layered fabrication can also be combined with subtractive micromachining in a printed circuit microelectrical mechanical system (PC-MEMS) process to create complex, three-dimensional mechanisms with sub-millimeter features, such as the monolithic bee robot [68].

This paper describes the fabrication process of using planar layers of carbon nanotube (CNT) composite material to form three-dimensional mechanisms and robotic components. The method is demonstrated through the fabrication of two novel meso-scale mechanisms—one which shows the design of a two-degree-of-freedom wrist mechanism intended for use in minimally invasive robotic surgical instruments, and another which shows the design of a two-degree-of-freedom gripping mechanism, also intended for robotic surgical procedures. A comparison is made between two variations of the first design in which different layer thicknesses are used to demonstrate how the tolerances of the part can be improved.

6.2 CNT Stacking Technique Overview

The CNT stacking technique consists of four main steps that will be described in further detail and are illustrated in Fig. 6.3.

- Lithographic patterning and growth of CNT frameworks
- Removal of the individual layers from the silicon substrate
- Stacking and alignment of the CNT composite layers

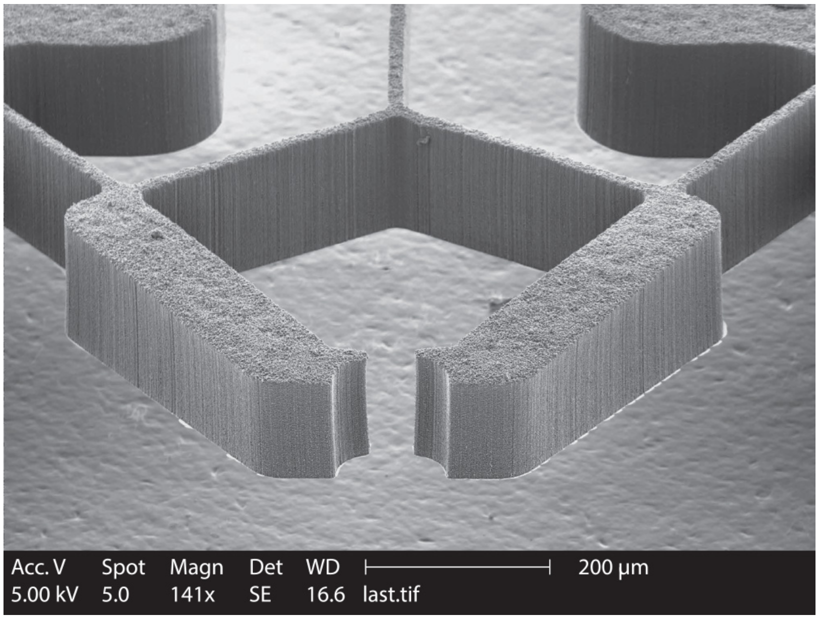

Figure 6.1: A CNT composite structure patterned using photolithography. The layer thickness shown here is approximately 100 μm.

- Bonding the composite layers to form the final 3D component

Carbon nanotube frameworks are lithographically patterned on a silicon wafer. Photolithography provides exceptionally good detail and resolution for features as small as tens of nanometers [69, 70]. Once the CNT frameworks are patterned they can be grown to thicknesses anywhere from 5 μm to approximately 700 μm. Thus, the process combines the micro scale precision of photolithography with the CNT growth process to produce millimeter-scale structures. Figure 6.1 shows a CNT composite mechanism that was patterned using photolithography.

The fabrication process used to create the CNT frameworks (step 1 in the overall process introduced here) is described in detail in [56, 71]. The initial growth of the CNT framework occurs on a silicon substrate (see Fig. 6.3(a)). A thin film of iron, generally 4-7 nm thick, is used as a growth catalyst. The carbon nanotubes grow perpendicularly, away from the substrate, to form a forest of nanotubes. This forest is fairly porous. The growth is followed by an infiltration process using chemical vapor deposition to create a CNT composite material. A number of materials can be used in the infiltration process including nickel, silicon, and carbon, depending on the desired material properties. Figure 6.2 shows a CNT forest that has been infiltrated with carbon. The frameworks for the examples presented in this paper are also infiltrated with carbon.

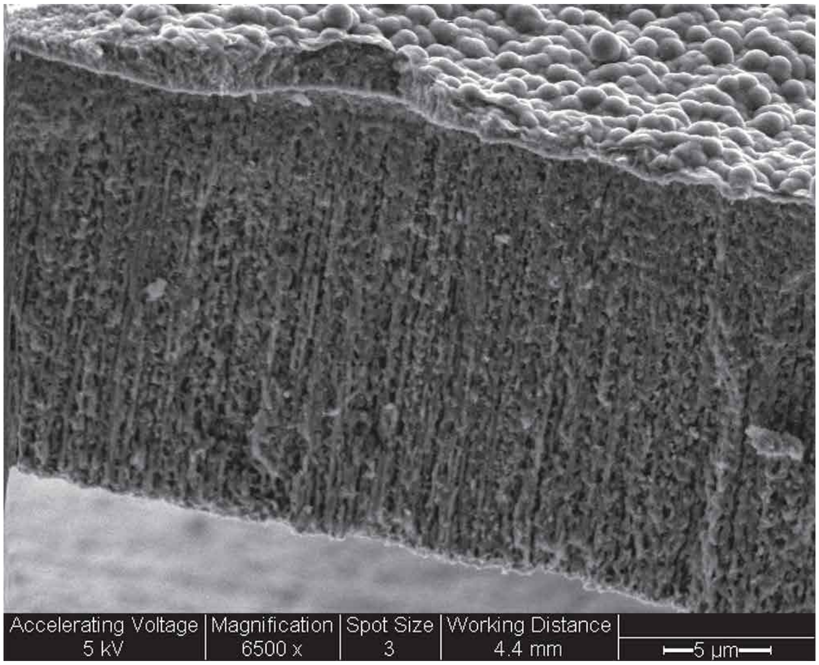

Figure 6.2: A sample of CNT forest that has been infiltrated with carbon. Because the carbon nanotubes are coated in carbon, they are more visible at this scale.

Once the framework has been infiltrated it is removed from the silicon wafer and the individual patterned layers are stacked to form the 3D assembly (Figs. 6.3(b) and 6.3(c)). To facilitate the stacking process and ensure proper alignment relative to the other layers, each layer is patterned with one or more square holes which fit over an alignment pin. This also helps keep them in place until they can be joined together. After the layers have been stacked to form the 3D structure, the layers are bonded together (Fig. 6.3(d)).

There are a few possible techniques for bonding the layers to form a single assembled part. One way is to use an adhesive that can be spread across all layers. This method is demonstrated in the mechanisms described later. Another method involves further infiltration with carbon using chemical vapor deposition. Once the layers are stacked together, they can be infiltrated again using the same infiltration process that was used to create the layers initially, thus bonding the layers to one another. This process was also tested and successfully demonstrated.

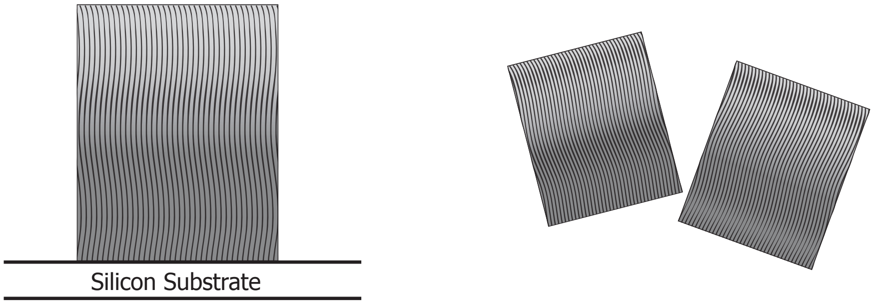

(a) Step 1: Lithographically pattern and infiltrate CNT composite layers (b) Step 2: Separate layers from silicon substrate

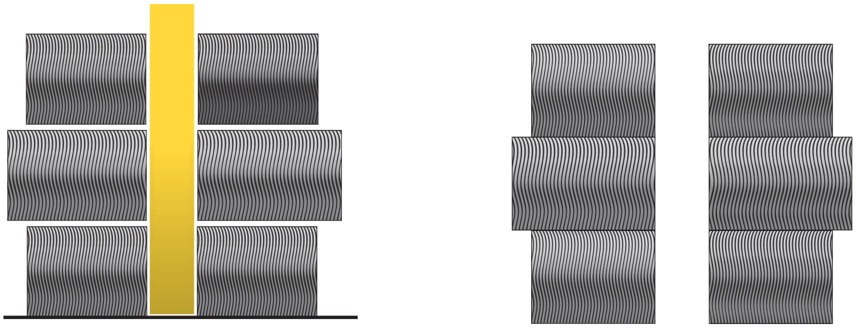

(c) Step 3: Stack layers using alignment pins (d) Step 4: Bond layers together and remove alignment pins

Figure 6.3: The process used to assemble the CNT composite layers after the growth and infiltration processes

6.3 Mechanism Design

Two mechanism designs are presented that are being developed for use in robotically-controlled surgical instruments. The first is a 2-DoF wrist mechanism—referred to as the Crossed Cylinder Wrist—which can be used to articulate a surgical end effector (forceps, cutting tool, cautery tool, etc.) through a large range of motion while occupying relatively little space. The second—referred to as the Split CORE Grips—is a mechanism which has two mating grips for grasping and manipulating objects and can be rotated in one degree of freedom.

Both mechanisms are designed to be attached to the end of an instrument shaft no larger than 3 mm in diameter. The mechanisms are actuated by cables in a pull-pull configuration. At the opposite end of the instrument, the cables interface with the robotic controls (see Fig. 6.4). De-

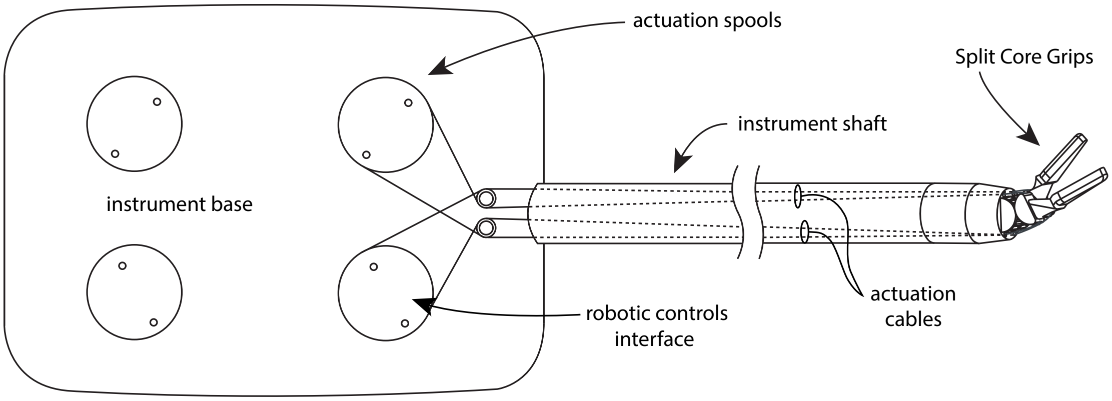

Figure 6.4: Schematic showing the end effector (Split CORE Grips shown here) attached to the end of the instrument shaft. Cables are set up in a pull-pull configuration and are robotically actuated at the base of the instrument.

signing a surgical instrument at this size scale requires fine feature resolution because the smallest features are on the order of tens of micrometers. However, the overall size must be large enough to serve as an effective surgical tool. For this reason, the CNT stacking technique is considered a good method to achieve the meso-scale qualities of these designs. Further, by reducing the size of surgical instruments surgeons are able to perform less invasive procedures that require shorter recovery times, less pain medications, and less scarring [58].

6.3.1 Crossed Cylinder Wrist

A 2-degree-of-freedom wrist is desirable because it allows a surgical instrument to be precisely controlled through a wide range of motion. The Crossed Cylinder Wrist is designed to reduce the number of parts required for wrist-like motion. It is also desirable that the wrist be compact and occupy a minimal volume as it moves through its extremes of motion. This allows the instrument to be used in small, confined spaces.

The motion of the Crossed Cylinder Wrist is controlled by gear profiles on two mating components that are held in compressive contact. The components are shaped as half cylinders and arranged so that the axis of one component is orthogonal to the axis of the other, as shown in Fig. 6.5. With one of the components held fixed to the shaft of the surgical instrument, the other component is able to roll along the surface of the fixed component. It can roll in the direction of

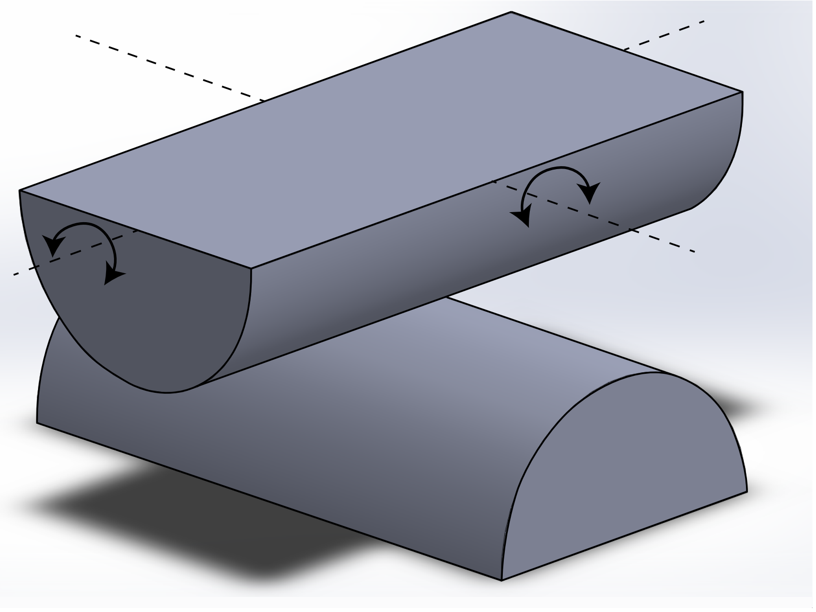

Figure 6.5: The upper cylinder is able to roll along the axial direction of the lower cylinder. It can also roll about the axis of the lower cylinder, as shown by the arrows.

the axis of the fixed component (first degree of freedom), and it can also roll around the axis of the fixed component (second degree of freedom).

The gear teeth are used to prevent sliding motion and to provide torsional and shear stability. Because the mechanism is designed to roll in two directions, the gear profile in the radial direction is that of a spur gear, and the profile along the axis of the half cylinder is that of a rack gear. However, rather than having a continuous spur gear profile along the axial direction, the spur gear profile is staggered to prevent sliding along the axial direction. By using gear teeth to guide the mechanism, motion is primarily constrained to rolling with little translation, or sliding, and the friction associated with motion is minimized. A model of one half cylinder with gear teeth is shown in Fig. 6.6.

6.3.2 Split CORE Grips

The Split CORE Grips are designed to minimize sliding friction between parts and maintain a high level of dexterity by providing motion in two degrees of freedom. The concept is inspired by a Compliant Rolling-Contact Element (CORE) which utilizes curved surfaces to guide the rolling motion of one component over the surface of the other component. In a traditional CORE joint the

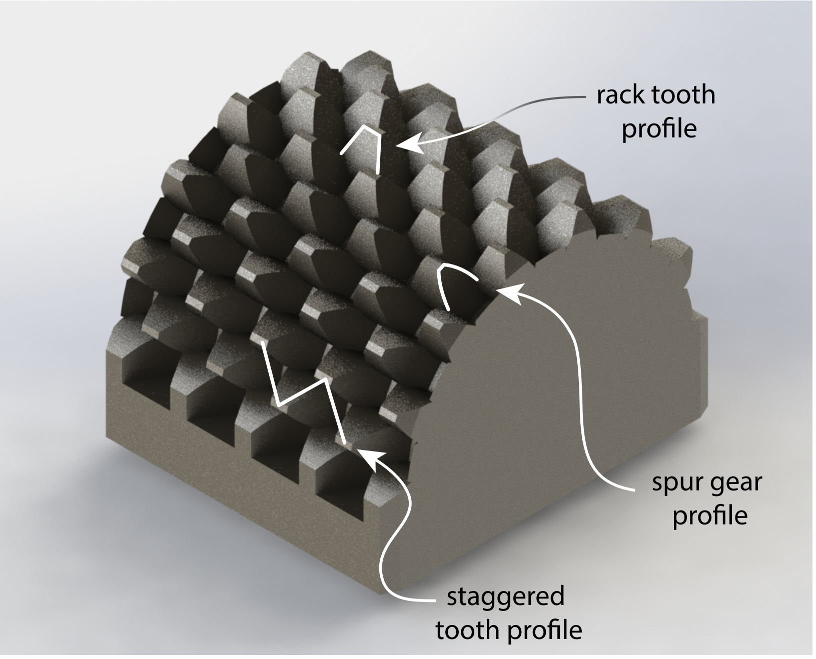

Figure 6.6: A rendering of a component for the Crossed Cylinder Wrist showing the two different gear profiles and the staggered tooth configurations to prevent torsion and shear.

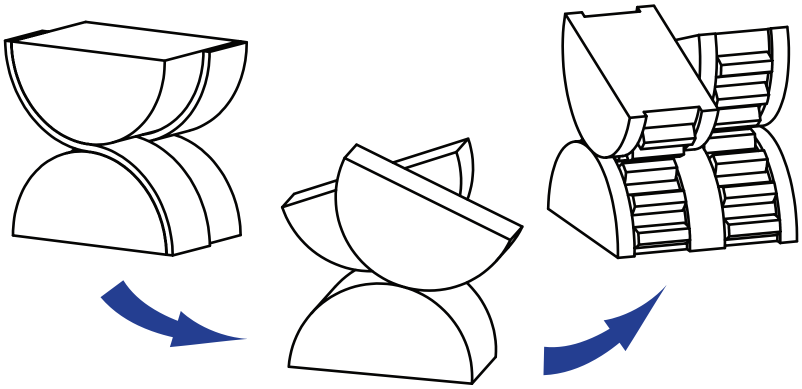

Figure 6.7: An illustration showing the similarities and distinctions between the traditional CORE joint (left) and the split CORE joint used in the gripping mechanism design (right).

motion is constrained by flexures attached to the upper and lower segments [3]. This ensures that the center of rotation is always at the point of contact between the two segments (see Fig. 6.7).

In contrast to the traditional CORE joint which relies on flexures to guide its motion, the mechanism described here uses an involute gear profile on the curved surfaces to allow rotation while preventing slipping motion. The mechanism described thus far consists of only a single upper component that moves relative to a lower base. To create a gripping mechanism, the upper segment can be split into two identical parts that are able to roll along the surface of the base part independently of one another. Grips are added to each of these upper components creating a gripping mechanism similar to the one shown in Fig. 6.8.

In this particular instrument design the grips are actuated by small cables that extend along a narrow shaft. The cables are attached to either side of the individual upper CORE segments, in a pull-pull configuration. Thus, the cables actuate the grips and the cable tension holds the assembly together, ensuring that the upper and lower segments are in compressive contact. Because a gear profile is used to guide the motion, it is important that the mating gear profiles maintain the proper spacing. Smooth, circular regions whose diameter is equal to the pitch diameter of the gear profile are included in the design to ensure proper spacing between the components. The circular regions also act as load-bearing surfaces, sustaining the compressive loads required to keep the grip components in contact with the base. This prevents the loads from being transmitted to the gear teeth.

6.4 Fabrication of Robot Components

Stacking layers of planar patterns is used to form 3D objects. The detail and level of precision of the object depends on how the cross sections of the object change in the direction of stacking. For example, a simple sphere could be created by stacking a series of different sized circular layers (see Fig. 6.9). However, the change in diameter from one layer to the next will produce a corner creating a rough surface on the sphere. The smoothness of the surface can be improved by decreasing the thickness of each layer so that the change in cross section from one layer to the next is gradual.

Other objects may be less prone to the effects of layer thickness if the cross section remains unchanged along the direction of stacking, or if the cross section changes are discrete. For example, in the Split CORE Grips design, there is an abrupt change in cross section when the smooth, circular surface transitions to the gear profile. This change in cross section is accommodated by stacking two layers with the different cross sections without any loss in the original detail of the part.

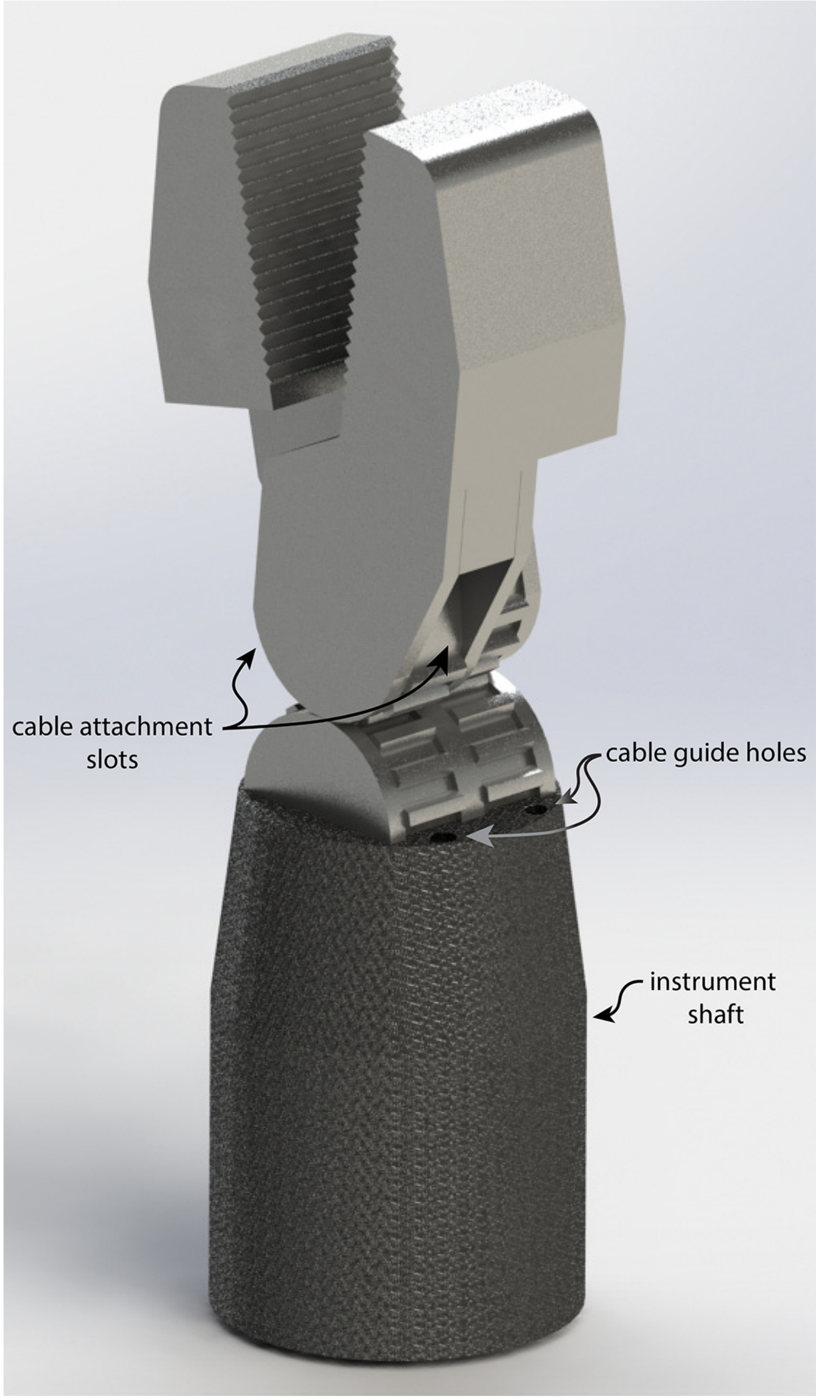

Figure 6.8: A rendering of the base component and the upper grip components of the Split CORE Grips

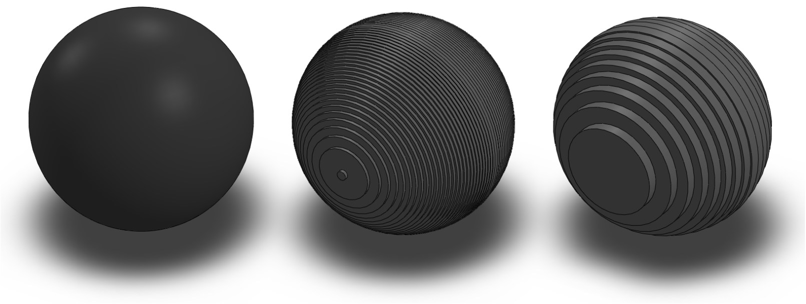

Figure 6.9: A rendering illustrating the effects of layer thickness on part definition. The desired part geometry (left), the layered assembly using layer thickness of 1 unit (middle), and the layered assembly using layer thickness of 3 units (right).

6.4.1 Crossed Cylinder Wrist

The direction of stacking for the Crossed Cylinder Wrist is along the respective axes of the half cylinders. Therefore, the spur gear profile (in the radial direction) is well defined by the lithographic patterning. However, the rack profile in the opposite direction will be defined by the thickness of the stacking layers. Thin layers will produce a gradual change in cross section and a well defined rack profile but will require a large number of layers. In contrast, a coarser design will require fewer layers in the assembly process but will produce a rough tooth profile. To show this contrast, two different models were constructed. One model contains 19 layers 110 μm thick. The results are shown in Figs. 6.10 and 6.11. The other, more detailed model contains 50 layers that are only 40 μm thick. Each individual layer for this model is shown in Fig. 6.12. After the individual layers were stacked on the alignment pin, cyanoacrylate adhesive was spread across the flat bottom surface to hold the layers in place. The assembled components are shown in Figs. 6.13 and 6.14. Figure 6.14 also shows a comparison between the mechanisms with the fine and coarse layer thickness.

6.4.2 Split CORE Grips

The cross section of the Split CORE Grips is mostly uniform but there are a few key characteristics that must be preserved in the layered assembly to ensure proper behavior. There are three of the smooth circular regions on the base segment. Each is identical so this portion of the

Figure 6.10: Optical micrograph of one portion of the Crossed Cylinder Wrist comprised of 19 layers that are 110 μm in thickness

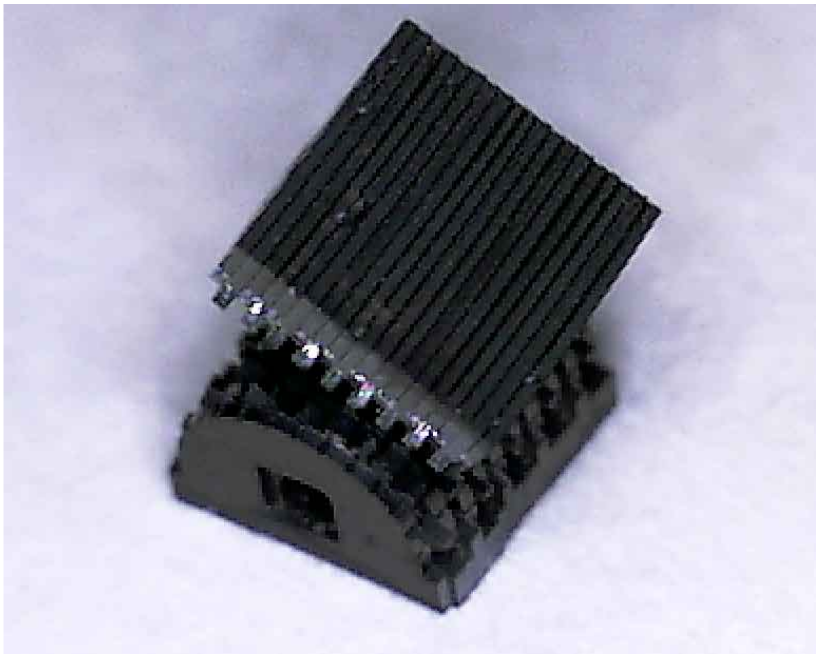

Figure 6.11: Micrograph of the assembled Crossed Cylinder Wrist with a more coarse stacking assembly (110 μm layer thickness). The upper piece is rotated slightly about the axis of the lower and rolled slightly forward to demonstrate both directions of motion.

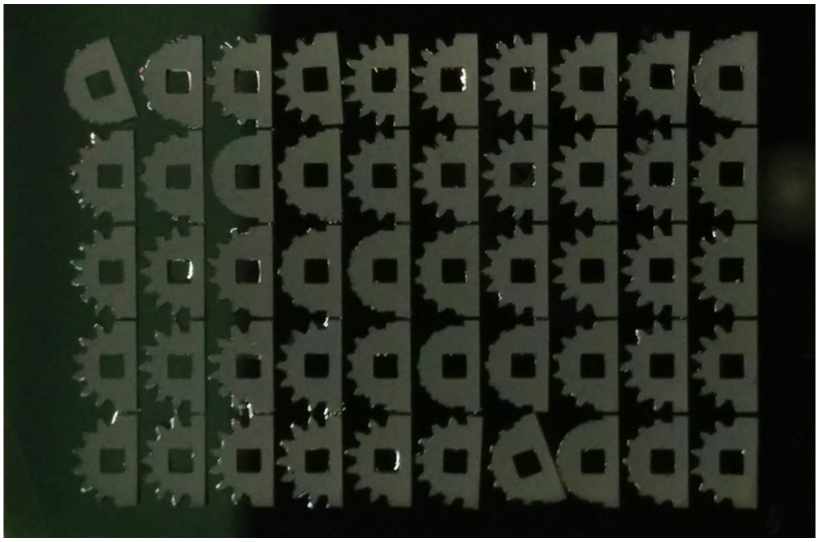

Figure 6.12: Example of individual CNT layers for the Crossed Cylinder Wrist prior to removing them from the silicon chip for assembly. Each layer is 40 μm in thickness.

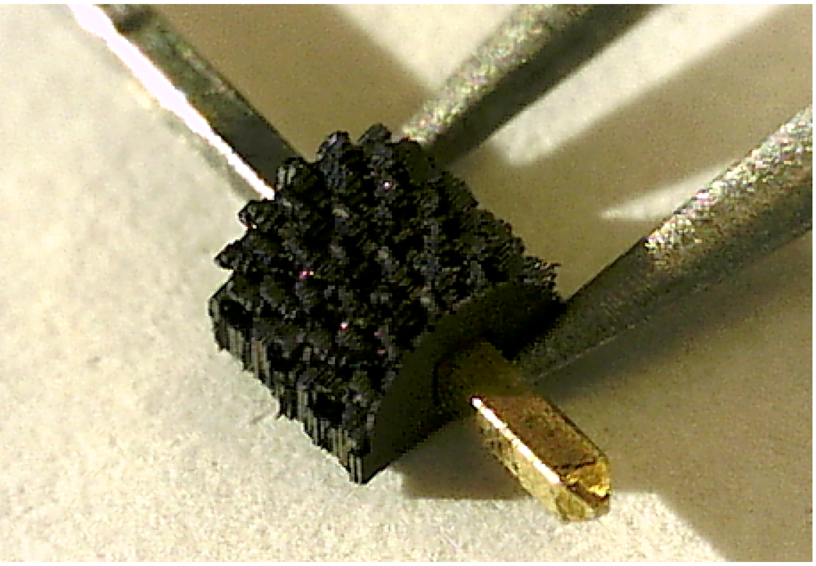

Figure 6.13: One portion of the Crossed Cylinder Wrist layers stacked on the alignment pin. The full assembly is comprised of 50 layers that are 40 μm in thickness.

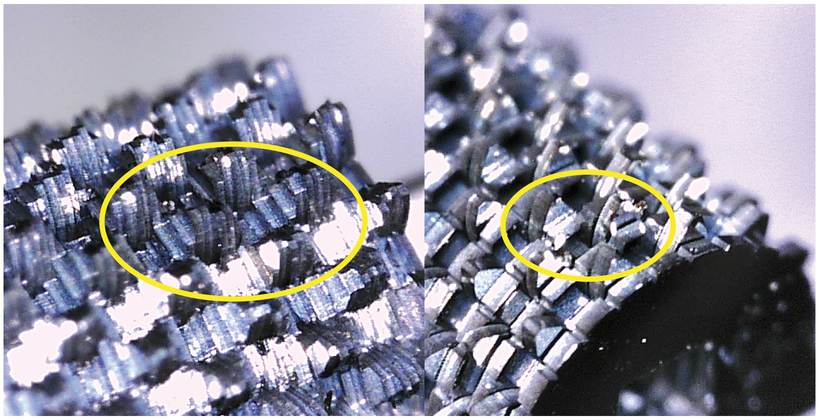

Figure 6.14: A comparison of the two Crossed Cylinder Wrist versions—40 μm (left) and 110 μm (right) layer thickness—showing how the profile along the direction of stacking improves with reduced layer thickness.

cross-section can simply be repeated three times in the lithography mask process. Second, the gear profile must be defined and is also repeated in the base segment. Lastly, a square is included in each layer so that the layers can be stacked together and aligned on the alignment pin used for assembly.

The upper segments, which include the grip surfaces, are slightly more complicated. They also consist of the smooth circular segments and the gear profile. Additionally, the grip must extend far enough to come in contact with the opposite grip. This portion of the grip creates an overhang that does not include the lower geared section of the body. Thus, the upper grip portion of the segment is the only part of the body that is common throughout the entire cross section so the square alignment hole is placed in this region. A second hole is included in the CORE portion of the body to more precisely align the gear profiles and smooth circular sections (see Fig. 6.15).

The resulting mechanism is well defined and simple to assemble. The Split CORE Grips design consists of three unique cross sections—the smooth circular surfaces, the geared portion, and the overhanging portion of the grips. There is no gradual change between these three cross sections. This makes the design well suited for the CNT layered assembly technique because the fidelity of the original design is completely retained. The assembled CNT layers of the base and two grips are shown in Figs. 6.16 and 6.17. Figure 6.17 shows the Split CORE Grips assembled atop the base component at the end of the instrument shaft (not shown). There are two actuating

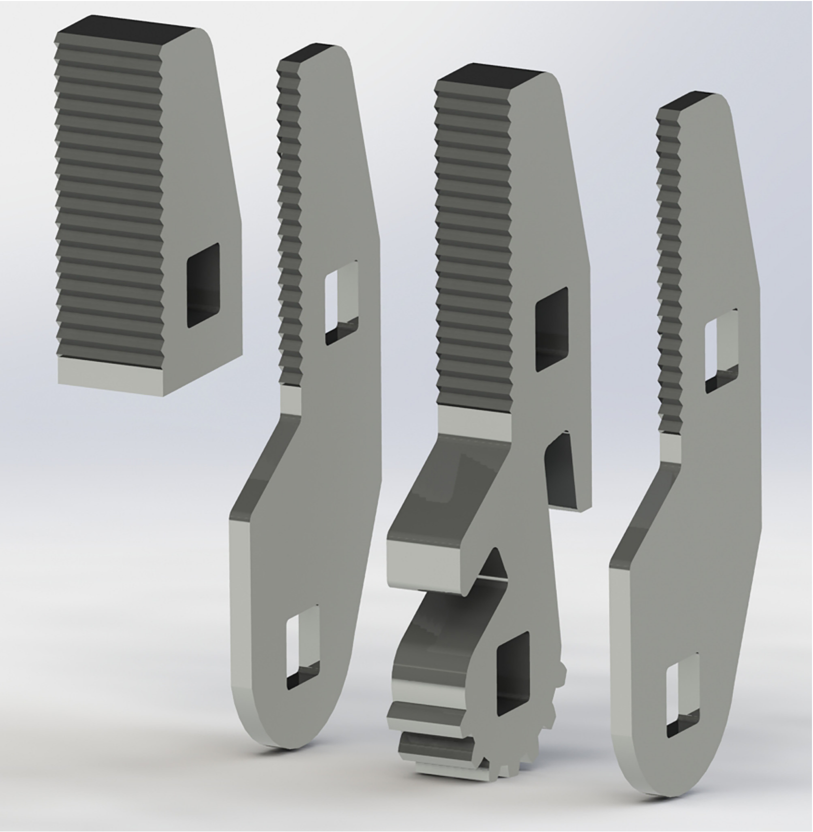

Figure 6.15: Rendering of the Split CORE Grips divided into the three unique layers and the square holes used for alignment. The smooth circular section is repeated on either side of the geared portion.

cables attached to each grip. The cables keep the grips in contact with the base component and allow the grips to be precisely controlled at any particular angle relative to the base.

6.5 Limitations

While the CNT patterning process uses photolithography to achieve micro-scale precision, the growth, stacking, and alignment processes introduce a certain amount of inaccuracy in the desired geometry. During the growth process the CNT frameworks can be grown to thicknesses in the range of 5 μm to approximately 700 μm. Within this range the desired height can generally be achieved within $\pm 10\%$. Thicknesses outside this range can be achieved but challenges begin to arise that make the process more difficult to accurately control. For thicknesses below 5 μm the accuracy is much lower because the growth time is much shorter ($<$ 5 sec). Therefore, the

Figure 6.16: Photograph of the assembled geared portion of the Split CORE Grips (left) and a view of all the assembled elements (base piece and two grips) of the mechanism (right).

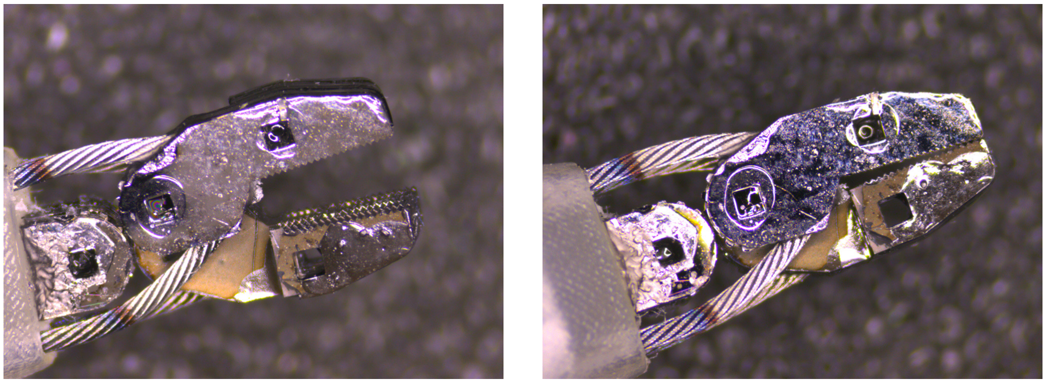

(a) Grips in partially open position

(b) Grips in closed position

Figure 6.17: Split CORE Grips assembled onto a surgical instrument shaft. Cables are used to actuate the grips to a desired angle. Each grip is controlled by two cables.

increased resolution in the direction of stacking that can be gained by using thinner CNT layers is somewhat offset by the inaccuracies in growth height as it approaches 5 μm.

Another source of error in the growth process arises when the sidewalls begin to slope inward or outward. This can be caused by a number of factors including iron catalyst thickness and growth height. Smaller iron layer thickness results in good edge definition but tapered walls, while larger iron layer thickness results in straighter walls but poorer edge definition [72]. The walls in the prototypes presented here generally slope outward and the angle of the walls was measured to be as high as 5°. Despite being a relatively small slope, this leads to measurable error, particularly in thick parts such as the geared portion of the Split CORE Grips. For a 700 μm layer, the 5° angle would lead to a deviation of 61 μm. To reduce error caused by sidewall taper, the iron catalyst thickness could be increased to 7 or 8 nm and support structures could be added to the lithography mask as shown in [72].

A third source of error, and perhaps the most significant, comes as a result of the stacking and alignment process. The square hole in each layer is designed to fit on the alignment pin but also have some space to allow easier placement on the pin and, eventually, removal from the pin. However, the slightly over-sized hole allows a small amount of rotation on the pin and leads to misalignment. Figure 6.13 shows one of the assemblies after stacking but prior to the final alignment procedure of pushing all of the layers against one side of the pin. While this does provide fairly good alignment, some parts shift as the assembly is removed from the pin or as adhesive is applied.

A possible solution to this problem is to design alignment holes with compliant features on adjacent sides of the square hole. They would be designed to deflect away enough to slide the part onto the pin but provide enough force to push the part to one corner of the pin once it has been placed. This would better align each of the layers relative to one another. These features could be designed into the lithography mask along with the support structures that help promote straight sidewalls.

6.6 Results and Conclusions

In addition to changes in the CNT composite material, the changes in geometry among the layers discussed previously are expected to improve the assembly process and minimize error.

This paper introduced a method of creating millimeter-scale robotically-controlled mechanisms using carbon-infiltrated CNT layers. The layers are patterned using photolithography, thus achieving fine resolution and detail. Two methods were discussed for joining the stacked layers of CNT composite—a surface bonding method using adhesive, and the formation of carbon bonds via chemical vapor deposition. Two designs for robotically-controlled surgical instruments were presented as sample parts that can be created using the patterned layer assembly technique. In

Crossed Cylinder Wrist, different layer thicknesses were used to demonstrate how reduced layer thickness can improve the detail and precision of the final assembled structure.

The Split CORE Grips and the Crossed Cylinders Wrist mechanisms were fabricated using the CNT stacking technique. Cables were attached to the assemblies for actuation (see Fig. 6.17) to demonstrate the motion of the mechanisms. They were able to be actuated but the compressive forces holding the parts together caused portions of the CNT material to fracture. In the future, additional prototypes will be fabricated using CNT material that is infiltrated for shorter times with carbon (2-4 min) followed by a nickel electroplating process. We anticipate that the new CNT carbon-nickel composite will provide greater strength and be able to better sustain the compressive forces required for actuation.

Despite the high resolution achieved through lithographic patterning, there are a number of challenges that lead to inaccuracies in the final assembly. The sources of these errors are associated with both the CNT growth process and the geometric design of the individual components. Solutions to these problems have been proposed for future work.

CHAPTER 7. CONCLUSION AND FUTURE WORK

7.1 Conclusions

The three concepts described in Chapters 3, 4, and 5 aim to fill various needs in the development of needlescopic surgical instruments. Smooth, wrist-like motion is desired to articulate an instrument in two directions of rotation. The Crossed Cylinders Wrist concept achieves this behavior while also minimizing the amount of volume the mechanism occupies. Simplified geometry and reduced part count are also key objectives in order to facilitate manufacturing and assembly on the millimeter scale. The Inverted Flexure Grips and the Split CORE Grips each provide grip and rotational motion while offering fairly simple geometries focused on fabrication feasibility. Other aspects of the three designs were also guided by the need to fulfill key performance objectives.

While none of the three concepts constitute a fully functional end effector comparable to current 5 and 8 mm designs with wrist and grip motion, they do offer insights into techniques for achieving such performance. They can, in a sense, be considered building blocks that can be combined with other concepts to achieve the full desired behavior of a surgical instrument. In future design iterations, the basis of these concepts can help inspire new designs that also address challenges of manufacturing, assembly, range of motion, and swept volume.

7.2 Thesis Summary

The intent of this research project was to generate and refine mechanism designs capable of functioning as surgical instruments on the 3 mm diameter size scale. The following has been performed in fulfillment of that objective:

- A literature review to assess current and prior work in the field
- Concept generation and analysis of three key concepts (Split CORE, Inverted Flexure, and Crossed Cylinders Wrist)

- Prototyping and testing of two of the three concepts to validate and compare results to hand calculations and finite element analyses

In addition to fulfillment of the research contract with Intuitive Surgical, Inc. another objective of this work was to contribute findings and developments to the scientific community through publications and patent applications. Chapter 5 was accepted and presented at the 3rd Conference on Microactuators and Micromechanisms in Timisoara, Romania, 2-4 October, 2014. Chapter 6 is has been submitted and is currently under review for the ASME Journal of Mechanisms and Robotics. Provisional patent applications have also been submitted for both the Split CORE Grips and the Crossed Cylinder Wrist concepts.

7.3 Future Work

The results of this work provide a foundation on which to 1) further test and refine existing concepts, 2) prototype and test additional concepts, and 3) establish design guidelines for small-scale instruments.

1. Further testing of existing concepts should include analysis of grip force throughout the range of motion, understanding of failure modes under various loading conditions, and mapping of cable position and velocity to grip position and velocity.
2. Prototyping of additional concepts could include concepts generated previously but not extensively analyzed or tested, such as the Oriceps mechanism. It may also include new concepts that have not yet been established.
3. Lastly, establishing design guidelines will provide an understanding of the relationships between key performance characteristics such as the correlation between yield strength and maximum grip force. These design guidelines would also give insight into instrument performance as a function of overall scale.

Focusing on these three areas will help Intuitive Surgical move closer to its goals of creating small diameter instruments and enabling new surgical procedures to be performed through robot-assisted surgery.

REFERENCES

[1] Intuitive Surgical Inc. Q3 Investor Presentation. Oct. 2013. http://www.intuitivesurgical.com/.

[2] Blum, C., and Adams, D., 2011. "Who did the first laparoscopic cholecystectomy?." *Journal of Minimal Access Surgery,* **7**(3), pp. 165–168.

[3] Halverson, P. A., Howell, L. L., and Magleby, S. P., 2010. "Tension-based multi-stable compliant rolling-contact elements." *Mechanism and Machine Theory,* **45**(2), pp. 147–156.

[4] Wang, X., Wang, S., Li, J., Zhang, G., and Wu, Z., 2013. "Conceptual design of a novel multi-DoF manual instrument for laparoscopic surgery." *The International Journal of Medical Robotics and Computer Assisted Surgery,* **9**(1), pp. 75–82.

[5] Whitman, M.P. et al. Surgical Device Having Multiple Drivers. US Patent 7963433 B2. Tyco Healthcare Group, assignee. 21 June, 2011.

[6] Jelinek, F., Pessers, R., and Breedveld, P., 2013. "Dragonflex-smart steerable laparoscopic instrument." *Journal of Medical Devices,* **7**, June, pp. 1–2.

[7] Hoxhold, B., and Bttgenbach, S., 2010. "Easily manageable, electrothermally actuated silicon micro gripper." *Microsystem Technologies,* **16**(8-9), pp. 1609–1617.

[8] Chen, W., and Lin, W., 2002. "A miniature gripper system for optical fiber handling." Vol. 4902, pp. 436–443.

[9] Fan, P. Laparoscopic Dual Grasper. US Patent 20120239080 A1. 20 Sept. 2012.

[10] Buysse, S.P. et al. Laparoscopic Bipolar Electrosurgical Instrument. US Patent 20030014052 A1. 16 Jan. 2003.

[11] Duval, E. F., 2012. Method and apparatus for reducing at least one friction force opposing an axial force exerted through an actuator element.

[12] Chojin, E.M. End Effector Assembly for Electrosurgical Device. Covidien, assignee. US Patent 8382792 B2. 26 Feb. 2013.

[13] Lutze, T. et al. Surgical Instrument. US Patent 20100160940 A1. Aesculap Ag, assignee. 24 June 2010.

[14] Hong, M. B., and Jo, Y. H., 2012. "Design and evaluation of 2-DoF compliant forceps with force-sensing capability for minimally invasive robot surgery." *Robotics, IEEE Transactions on,* **28**(4), pp. 932–941.

[15] Krpata, D., and Ponsky, T., 2013. "Needlescopic surgery: whats in the toolbox?." *Surgical Endoscopy,* **27**(3), pp. 1040–1044.

[16] Aguirre, M. E., and Frecker, M., 2008. “Design innovation size and shape optimization of a 1.0 mm multifunctional forceps-scissors surgical instrument.” *Journal of Medical Devices,* **2**(1), Mar.

[17] Aguirre, M. E., Hayes, G. R., Meirom, R. A., Frecker, M. I., Muhlstein, C. L., and Adair, J. H., 2011. “Optimal design and fabrication of narrow-gauge compliant forceps.” *Journal of Mechanical Design,* **133**(8), Aug.

[18] Canfield, S., Edinger, B., Frecker, M. I., and Koopmann, G. H., 1999. “Design of a piezoelectric inchworm actuator and compliant end effector for minimally invasive surgery.” Vol. 3668, pp. 835–843.

[19] Jung, G.-P., Koh, J.-S., and Cho, K.-J., 2011. “Meso-scale compliant gripper inspired by caterpillar’s proleg.” In *Robotics and Automation (ICRA), 2011 IEEE International Conference on*, pp. 1831–1836.

[20] Chiel, H.J. et al. Biologically Inspired Gripping Device. Case Western Reserve University, assignee. US Patent 8500179 B2. 6 Aug. 2013.

[21] Roch, I., Bidaud, P., Collard, D., and Buchaillot, L., 2003. “Fabrication and characterization of an SU-8 gripper actuated by a shape memory alloy thin film.” *Journal of Micromechanics and Microengineering,* **13**, pp. 330–336.

[22] Franken, M., 2003. “Smart memory alloy actuated slave system for medical robotics, with haptic feedback.” Master’s thesis, Eindhoven University of Technology.

[23] Morra, F., Molfino, R., and Cepolina, F., 2004. “Miniature gripping device.” In *Proc. of IEEE International Conference on Intelligent Manipulation and Grasping*.

[24] Sall, D., Cepolina, F., and Bidaud, P., 2004. “Surgery grippers for minimally invasive heart surgery.” In *Proc. of IEEE International Conference on Intelligent Manipulation and Grasping*.

[25] Kode, V., Cavusoglu, M., and Azar, M., 2005. “Design and characterization of a novel hybrid actuator using shape memory alloy and DC motor for minimally invasive surgery applications.” In *Mechatronics and Automation, 2005 IEEE International Conference*, Vol. 1, pp. 416–420.

[26] Eisinberg, A., Tonet, O., Dario, P., Macri, G., and Carrozza, M., 2006. “Microfabricated instruments for fetal cardiac surgery: Experiments on haptic tissue recognition.” In *Haptic Interfaces for Virtual Environment and Teleoperator Systems, 2006 14th Symposium on*, pp. 273–279.

[27] Saedi, S., Mirbagheri, A., and Farahmand, F., 2011. “Conceptual design of a miniaturized hybrid local actuator for minimally invasive robotic surgery (MIRS) instruments.” In *Engineering in Medicine and Biology Society,EMBC, 2011 Annual International Conference of the IEEE*, pp. 2140–2143.

[28] Nah, S., and Zhong, Z., 2007. “A microgripper using piezoelectric actuation for micro-object manipulation.” *Sensors and Actuators A: Physical,* **133**(1), pp. 218–224.

[29] Park, J., and Moon, W., 2003. "A hybrid-type micro-gripper with an integrated force sensor." *Microsystem Technologies,* **9**(8), pp. 511–519.

[30] Keoschkerjan, R., and Wurmus, H., 2002. "A novel microgripper with parallel movement of gripping arms." In *Proceedings of the Eighth International Conference on New Actuators*, pp. 321–324.

[31] Krecinic, F., Duc, T. C., Lau, G. K., and Sarro, P. M., 2008. "Finite element modelling and experimental characterization of an electro-thermally actuated silicon-polymer micro gripper." *Journal of Micromechanics and Microengineering,* **18**(6).

[32] Zubir, M. N. M., and Shirinzadeh, B., 2009. "Development of a high precision flexure-based microgripper." *Precision Engineering,* **33**(4), pp. 362–370.

[33] Martinez, J. A., and Panepucci, R. R., 2007. "Design, fabrication, and characterization of a microgripper device." In *Florida Conference on Recent Advances in Robotics*.

[34] Liu, X., Tong, J., and Sun, Y., 2007. "Millimeter-sized nanomanipulator with sub-nanometer positioning resolution and large force output." In *Nanotechnology, 2007. IEEE-NANO 2007. 7th IEEE Conference on*, pp. 454–457.

[35] Kim, K., Liu, X., Zhang, Y., and Sun, Y., 2008. "Micronewton force-controlled manipulation of biomaterials using a monolithic MEMS microgripper with two-axis force feedback." In *Robotics and Automation, 2008. ICRA 2008. IEEE International Conference on*, pp. 3100–3105.

[36] Kim, D.-H., Lee, M. G., Kim, B., and Sun, Y., 2005. "A superelastic alloy microgripper with embedded electromagnetic actuators and piezoelectric force sensors: a numerical and experimental study." *Smart Materials and Structures,* **14**.

[37] Beyeler, F., Neild, A., Oberti, S., Bell, D., Sun, Y., Dual, J., and Nelson, B., 2007. "Monolithically fabricated microgripper with integrated force sensor for manipulating microobjects and biological cells aligned in an ultrasonic field." *Microelectromechanical Systems, Journal of,* **16**(1), pp. 7–15.

[38] Zubir, M. N. M., Shirinzadeh, B., and Tian, Y., 2009. "A new design of piezoelectric driven compliant-based microgripper for micromanipulation." *Mechanism and Machine Theory,* **44**(12), pp. 2248–2264.

[39] Duc, T. C., Creemer, J. F., and Sarra, P. M., 2006. "Lateral nano-newton force-sensing piezoresistive cantilever for microparticle handling." *Journal of Micromechanics and Microengineering,* **16**.

[40] Zoppi, M., Sieklicki, W., and Molfino, R., 2008. "Design of a microrobotic wrist for needle laparoscopic surgery." *Journal of Mechanical Design,* **130**(10), Sept., pp. 102306–102306.

[41] Marcincin, J. N., and Smrcek, J., 1997. "Biomechanical grippers: important elements of biomechanical robots." *Industrial Robot: An International Journal,* **24**, pp. 234–238.

[42] Zhao, B., and Nelson, C. A., 2013. "Decoupled cable-driven grasper design based on planetary gear theory." *Journal of Medical Devices,* **7**(2), June, pp. 020918–020918.

[43] Mei, F., Yili, F., Bo, P., and Xudong, Z., 2012. "An improved surgical instrument without coupled motions that can be used in robotic-assisted minimally invasive surgery." *Proceedings of the Institution of Mechanical Engineers, Part H: Journal of Engineering in Medicine,* **226**(8), pp. 623–630.

[44] Manzo, S., and Heaton, L., 2005. Wristed robotic surgical tool for pluggable end-effectors.

[45] Cooper, T. G., and Anderson, S. C., 2012. Flexible wrist for surgical tool.

[46] Yan Nai, T., Tuijthof, G. J. M., and Herder, J. L., 2011. "Steerable mechanical joint for high load transmission in minimally invasive instruments." *Journal of Medical Devices,* **5**(3), Sept.

[47] Howell, L., Magleby, S., and Olsen, B., 2013. *Handbook of Compliant Mechanisms*. New York, Wiley.

[48] Rogers, T. W., and Williams, M. R., 2008. Roll joint and method for a surgical apparatus.

[49] Wang, X., Wang, S., Li, J., Zhang, G., and He, C., 2012. "Easy grasp: A novel hybrid-driven manual medical instrument for laparoscopic surgery." *Proceedings of the Institution of Mechanical Engineers, Part C: Journal of Mechanical Engineering Science,* **226**(12), pp. 2990–3001.

[50] Lassooij, J., Tolou, N., Tortora, G., Caccavaro, S., Menciassi, A., and Herder, J., 2012. "A statically balanced and bi-stable compliant end effector combined with a laparoscopic 2DoF robotic arm." *Journal of Mechanical Sciences,* **3**, pp. 85–93.

[51] Peirs, J., Reynaerts, D., and Brussel, H. V., 2000. "Design of miniature parallel manipulators for integration in a self-propelling endoscope." *Sensors and Actuators A: Physical,* **85**(1-3), pp. 409–417.

[52] Budynas, R. G., and Nisbett, J. K., 2011. *Shigley's Mechanical Engineering Design, Ninth Edition*. McGraw-Hill.

[53] Howell, L. L., 2001. *Compliant Mechanisms*. John Wiley & Sons, Inc., New York, NY.

[54] Homer, E.R., Harris, M.B., Zirbel, S.A., Kolodziejska, J.A., Kozachkov, H. Trease, B.P., Borgonia, J.C., Agnes, G.S., Howell, L.L., and Hofmann, D.C., 2014. "New methods for developing and manufacturing compliant mechanisms utilizing bulk metallic glass." *Advanced Engineering Materials*.

[55] Hiller, J. et al. Bidirectional Gear, Method, and Applications. Cornell University, assignee. US Patent 20130055838 A1. 7 Mar. 2013.

[56] Toone, N. C., Fazio, W. F., Lund, J. M., Teichert, G. H., Jensen, B. D., Burnett, S. H., and Howell, L. L., 2014. "Investigation of unique carbon nanotube cell restraint compliant mechanisms." *Mechanics-Based Design of Structures and Machines,* **42**(3), pp. 343 – 354.

[57] Senapati, S., Advincula, A. P., 2007. "Surgical techniques: robot-assisted laparoscopic myomectomy with the da Vinci surgical system." *Journal of Robotic Surgery,* **1**(1), pp. 69–74.

[58] Yee, D. S., Shanberg, A. M., Duel, B. P., Rodriguez, E., Eichel, L., and Rajpoot, D., 2006. "Initial comparison of robotic-assisted laparoscopic versus open pyeloplasty in children." *Urology,* **67**(3), pp. 599 – 602.

[59] Pallav, K., Han, P., Ramkumar, J., Nagahanumaiah, and Ehmann, K. F., 2013. "Comparative assessment of the laser induced plasma micromachining and the micro-EDM processes." *Journal of Manufacturing Science and Engineering,* **136**(1).

[60] Spearing, S., 2000. "Materials issues in microelectromechanical systems (MEMS)." *Acta Materialia,* **48**(1), pp. 179 – 196.

[61] Hoople, G. D., Rolfe, D. A., McKinstry, K. C., Noble, J. R., Dornfeld, D. A., and Pisano, A. P., 2014. "Comparison of microscale rapid prototyping techniques." *Journal of Micro and Nano-Manufacturing,* **2**(3).

[62] Jabbari, E.; Rocheleau, D. N.; Xu, W.; He, X., 2007. "Fabrication of biomimetic scaffolds with well-defined pore geometry by fused deposition modeling." In *International Manufacturing Science and Engineering Conference*, pp. 71–76.

[63] Feygin, M; Hsieh, B., 1991. "Laminated object manufacturing: A simpler process." In *Proceedings of Solid Freeform Fabrication Symposium*, Austin, Texas.

[64] Kumar, A. V., Dutta, A., 2004. "Electrophotographic layered manufacturing." *Journal of Manufacturing Science and Engineering,* **126**(3), pp. 571–576.

[65] United States Patent 8,729,916. Methods of creating probe structures from a plurality of planar layers, 2014, Microfabrica, Inc.

[66] Waurzyniak, P. Micro Manufacturing Keeps Shrinking the Envelope, January, 2013 www.ManufacturingEngineeringMedia.com.

[67] Felton, S., Tolley, M., Demaine, E., Rus, D., and Wood, R., 2014. "A method for building self-folding machines." *Science,* **345**(6197), pp. 644–646.

[68] Sreetharan, P. S., Whitney, J. P., Strauss, M. D., Wood, R. J., 2012. "Monolithic fabrication of millimeter-scale machines." *Journal of Micromechanics and Microengineering,* **22**(5).

[69] La Fontaine, B., 2010. "Laser's and Moore's law." *SPIE Professional*, Oct., p. 20.

[70] Lin, B., 2009. *Optical Lithography.* SPIE Press, Bellingham, WA.

[71] Hutchison, D., Morrill, N., Aten, Q., Turner, B. W., Jensen, B. D., Howell, L., Vanfleet, R., and Davis, R., 2010. "Carbon nanotubes as a framework for high-aspect-ratio MEMS fabrication." *Microelectromechanical Systems, Journal of,* **19**(1), pp. 75–82.

[72] Moulton, K., Morrill, N., Konneker, A., Jensen, B., Vanfleet, R., Allred, D., and Davis, R., 2012. "Effect of iron catalyst thickness on vertically aligned carbon nanotube forest straightness for CNT-MEMS." *Journal of Micromechanics and Microengineering,* **22**(5).